Soil CO_2 emission and stable isotopes ($\delta^{13}C$, $\delta^{18}O$) of CO_2 and calcites reveal the fluid origin and thermal energy in the supercritical geothermal system of Krafla, Iceland

Giulio Bini [a,*], Giovanni Chiodini [a], Tullio Ricci [b], Alessandra Sciarra [b], Stefano Caliro [c], Anette K. Mortensen [d], Marco Martini [e], Andrew Mitchell [f], Alessandro Santi [c], Antonio Costa [a]

[a] Istituto Nazionale di Geofisica e Vulcanologia, Sezione di Bologna, viale Berti Pichat 6/2, 40127 Bologna, Italy
[b] Istituto Nazionale di Geofisica e Vulcanologia, Sezione Roma 1, via di Vigna Murata 605, 00143 Roma, Italy
[c] Istituto Nazionale di Geofisica e Vulcanologia, Osservatorio Vesuviano, Sezione di Napoli, via Diocleziano 328, 80124 Napoli, Italy
[d] Landsvirkjun, Háaleitisbraut 68, 103 Reykjavík, Iceland
[e] West Systems, via Don Mazzolari 25, 56025 Pontedera, Italy
[f] Lancaster Environment Centre, Lancaster University, LA1 4YQ Lancaster, United Kingdom

ARTICLE INFO

ABSTRACT

The Krafla geothermal system is located within a volcanic center that periodically erupts basaltic lavas, and has recently attracted an economic interest due to supercritical fluids forming near a shallow magma intrusion ($\sim$ 2 km depth). Here, we discuss new soil CO_2 flux and stable isotope data of the CO_2 efflux ($\delta^{13}C$) and hydrothermal calcites ($\delta^{13}C$, $\delta^{18}O$) of drill cuttings to estimate both the current magmatic outgassing from soils and the thermal flows in the geothermal system. Soil CO_2 emission is controlled by tectonics, following the NNE-SSW fissure swarm direction and a WSW-ENE trend, and accounts for $\sim$62.5 t d^{-1}. While the $\delta^{18}O$ of the H_2O in equilibrium with deep calcites is predominantly meteoric, both the $\delta^{13}C$ of the soil CO_2 efflux and of the fluids from which calcite precipitated have a clear magmatic origin, overlapping the $\delta^{13}C$ estimated for the Icelandic mantle (-2.5 ± 1.1 ‰). Estimates based on the soil CO_2 emission from the southern part of the system show that these fluxes might be sustained by the ascent and depressurization of supercritical fluids with a thermal energy of $\sim$800 MW. Such significant amount of energy might reach 1.5 GW if supercritical conditions extended below the whole investigated area. Finally, we report an increase in the soil CO_2 emission of about 3 times with respect to 14 years ago, likely due to recent changes in the fluid extracted for power production or magmatic activity. Pairing the soil CO_2 emission with stable isotopes of the efflux and calcite samples has important implications for both volcano monitoring and geothermal exploration, as it can help us to track magmatic fluid upflows and the associated thermal energy.

1. Introduction

Carbon dioxide is one of the predominant gases emitted by active volcanoes and geothermal systems, and the quantification of its emission and properties is fundamental for volcano monitoring and global budget for climatology. Due to its abundance and low solubility in silicate melts, it is one of the first gas species that escapes the magma reservoir during degassing (Giggenbach, 1996) and enters the overlying geothermal system. There, heat loss from shallow magmatic intrusions drives fluid convection of predominant meteoric origin, boiling, and steam separation (Hayba and Ingebritsen, 1997). The CO_2 preferentially partitioned into this vapor phase flows towards the surface up to the atmosphere through fumarolic vents and from soils (Chiodini et al., 2021).

The CO_2 emitted through diffusion from volcanic and geothermal soils accounts for a large part of the global budget of volcanic emissions (Werner et al., 2019). Its measurement enables us not only to quantify the magmatic-hydrothermal C release, but also to map the fracture network of the volcanic edifice from which fluids preferentially ascend (Chiodini et al., 1998). Changes in both extent and amount of CO_2 diffuse degassing from the soils of magmatic-hydrothermal systems may imply phases of volcanic unrest, potentially caused by new intrusions or episodes of magmatic outgassing. For example, the soil CO_2 emission

from the Campi Flegrei caldera (Italy) nearly quadrupled (from ~750 to 2800 t d^{-1}) and the areal extent of degassing became two times higher between 1998 and 2016, revealing the escalation of an unrest phase (Cardellini et al., 2017). Nevertheless, variations in the natural soil CO_2 emission from productive magmatic-hydrothermal systems may also be observed after changes in the mass and enthalpy of fluids extracted for power production. This is mainly ascribed to pressure drawdown or buildup in the productive geothermal aquifer. For example, the Reykjanes geothermal system (Iceland) registered a ~ 4× increase in the soil CO_2 emission from 2004 to 2013 (from 13.5 to 51.4 t d^{-1}), after installation of a 100 MWe geothermal power plant in 2006 (Óladóttir and Friðriksson, 2015).

The amount of CO_2 emitted into the atmosphere from soils can also be used to compute the mass and thermal flows in the subsurface of a hydrothermal system, thus resembling a useful indicator for geothermal exploration (Chiodini et al., 2021). Geothermal areas characterized by a good spatial correlation between soil temperature and CO_2 flux reflect the evidence of boiling zones in the subsurface, from which geothermal vapors with CO_2 separate. In these areas, the soil CO_2 emission can be used together with fumarole gas/steam ratios to compute the mass flow of the separated vapor and the thermal energy released through subsurface condensation (Chiodini et al., 2005; Fridriksson et al., 2006; Bini et al., 2019). Moreover, if the CO_2 content in the liquid is known from exploratory or productive wells, from the CO_2 emission we can also gain insights into the thermal energy of the upflowing liquid from which CO_2 separates through boiling (Chiodini et al., 2007; Bini et al., 2019).

To better quantify and monitor the soil CO_2 degassing, measuring the C isotopes of the efflux ($\delta^{13}C_{CO2}$) can be fundamental (Chiodini et al., 2008; Bini et al., 2020; Viveiros et al., 2020), as the very different isotopic signature of the CO_2 sources enables us to discriminate the effective magmatic C contribution. Soil gas respiration produces a CO_2 with very negative $\delta^{13}C$ (mean $\delta^{13}C_{CO2}$ ~ −27 ‰ and − 13 ‰ for C3 and C4 plants, respectively; Cheng, 1996), whereas magmatic degassing from divergent plate boundaries is thought to produce less negative values (upper mantle $\delta^{13}C_{CO2} = -5 \pm 1$ ‰, Marty and Zimmermann, 1999). Since C isotopes may fractionate during some processes occurring within the magmatic-hydrothermal system (e.g., magmatic degassing, calcite precipitation, mixing with surface water), the $\delta^{13}C$ stored in deep calcites precipitated from the hydrothermal fluid may help us to better understand the magmatic source of the CO_2 (Simmons and Christenson, 1994; Chiodini et al., 2015a). Furthermore, if the hydrothermal calcites are recovered at increasing depth during geothermal well drilling, from changes in their $\delta^{13}C$ one can gain new insights into the processes affecting the magmatic fluid upflow and the anatomy of the geothermal field.

Most of the CO_2 emitted from the magmatic-hydrothermal systems of Iceland is thought to reflect the decompression degassing of basaltic magmas as they ascend from the mantle to the upper crust (e.g., Ranta et al., 2023). This mantle CO_2 has been estimated to have a $\delta^{13}C$ of −2.5 ± 1.1 ‰ (Barry et al., 2014), and it constitutes the predominant component in the geothermal fluids of Iceland (Sano et al., 1985; Poreda et al., 1992; Barry et al., 2014; Ranta et al., 2023). Secondary processes can partly change both the abundance and the isotopic composition of this magmatic CO_2 in geothermal fluids, whereas fluids not associated with the active volcanic systems of Iceland exhibit a very wide range of $\delta^{13}C$. The variability of the $\delta^{13}C$ values of the Icelandic groundwaters (from −27.4 to +2 ‰) has been attributed to various processes, including air-water CO_2 exchange at the surface, dissolution of partially degassed basaltic rocks, precipitation of carbonate minerals, changes in the speciation of aqueous species upon water-rock reactions, and the introduction of magmatic gas into groundwater systems (Stefánsson et al., 2016, 2017).

The Krafla caldera (NE Iceland) hosts a geothermal system exploited since the 1970s in the vicinity of an active rift, which led to basaltic fissure eruptions and significant emissions of CO_2 during the last rifting episode of 1975–1984 (Einarsson, 1991). Monitoring the soil CO_2

emission and investigating the magmatic fluid contribution to the hydrothermal system is therefore fundamental for both volcanic surveillance and geothermal production. Since 1974, 43 geothermal wells have been drilled in that area, and together with geochemical and geophysical studies revealed insightful information about the geothermal fluid circulation in the subsurface (e.g., Mortensen et al., 2015; Árnason, 2020; Scott et al., 2022). Recently, two wells intercepted rhyolitic melt pockets at shallow depth (around 2 km) and supercritical fluids,[1] sparking interest in their very high energy content (3200 kJ kg^{-1}; Ingason et al., 2014) for electricity generation. Since 1974, the geothermal resource is extracted for electric power production through two turbines for a total of 60 MWe (Mortensen et al., 2015). The pre-production natural degassing state of the system is unknown, but soil CO_2 surveys carried out between 2004 and 2008 (Ármannsson et al., 2007; Dereinda and Armannsson, 2010), and the budget of CO_2 stored in hydrothermal calcites (Wiese et al., 2008), provided insights into the diffuse degassing from Krafla. Although changes in the geothermal productivity and the occurrence of a recent inflation-deflation of the ground (2018–2020) suggest possible variations in the subsurface fluid flow, the natural CO_2 emission has not been investigated in detail since 2008.

In this study, we measured new soil CO_2 fluxes with the accumulation chamber method (summer 2022) and analyzed stable isotopes of both efflux ($\delta^{13}C$) and hydrothermal calcites ($\delta^{13}C$, $\delta^{18}O$) to assess the current natural degassing of the geothermal field and the potential control of magma degassing on the CO_2 emission. $\delta^{13}C$ of the calcite samples recovered down to 1400 m depth from geothermal wells, including the two ones drilled into magma (IDDP-1 and KJ-39), shed light into the origin of geothermal C, which is consistent with that of the CO_2 currently emitted into the atmosphere. By combining the CO_2 emission with the chemical composition of the supercritical fluids, tapped near shallow magma intrusions, we show that a significantly high amount of thermal energy might upflow from the root of the Krafla geothermal system and feed the soil CO_2 fluxes. Finally, by comparing the CO_2 emission with that measured in the same area between 2004 and 2008, we found out an increase of about 3 times in 2022. The possible causes of this variation are discussed.

2. Geologic setting and previous soil CO_2 emission estimates

The Krafla volcano has a diameter of about 20 km and is located in northeast Iceland over a 90-km-long NNE-SSW fissure swarm (Fig. 1). Krafla, together with four other active volcanoes (Kverkfjöll, Askja, Fremrinámur, and Theistareykir) forms the northern volcanic zone (NVZ), which reflects the neovolcanic rifting activity (Einarsson, 2008; Hjartardóttir et al., 2016). An 8–10 km-wide caldera formed in the Krafla volcano about 110 ka during explosive volcanic activity (Fig. 1), which produced silicic tuff layers (Sæmundsson, 1991; Mortensen et al., 2015). Recent magmatic activity is predominantly basaltic, but rhyolites

---

[1] In this work, we use the term supercritical fluids for those fluids that exceed the supercritical temperature (T$_c$ = 374 °C), despite their pressure can be lower than the supercritical pressure (P$_c$ = 220 bar), such as the IDDP-1 fluids (440 °C and 140 bar; Heřmanská et al., 2019). These fluids are often referred to as superheated. This supercritical definition is in agreement with that previously adopted for Krafla fluids by Heřmanská et al. (2019), supporting that the superheated/supercritical differences can be semantic rather than physical and that fluid density must be taken into account (Driesner, 2021). Indeed, the state of water can change from superheated to supercritical on the same isocore (same density line) when temperature increases (Fig. 1 in Driesner, 2021), but no important changes in fluid properties have essentially occurred. In addition, since the fluid encountered during IDDP-1 drilling is a dilute fluid dominated by meteoric water, we can refer to the supercritical state of pure water at 374 °C. The addition of other constituents, such as NaCl, would instead generate significant changes in the T and P at which phase changes occur (Driesner and Heinrich, 2007; Driesner, 2021).
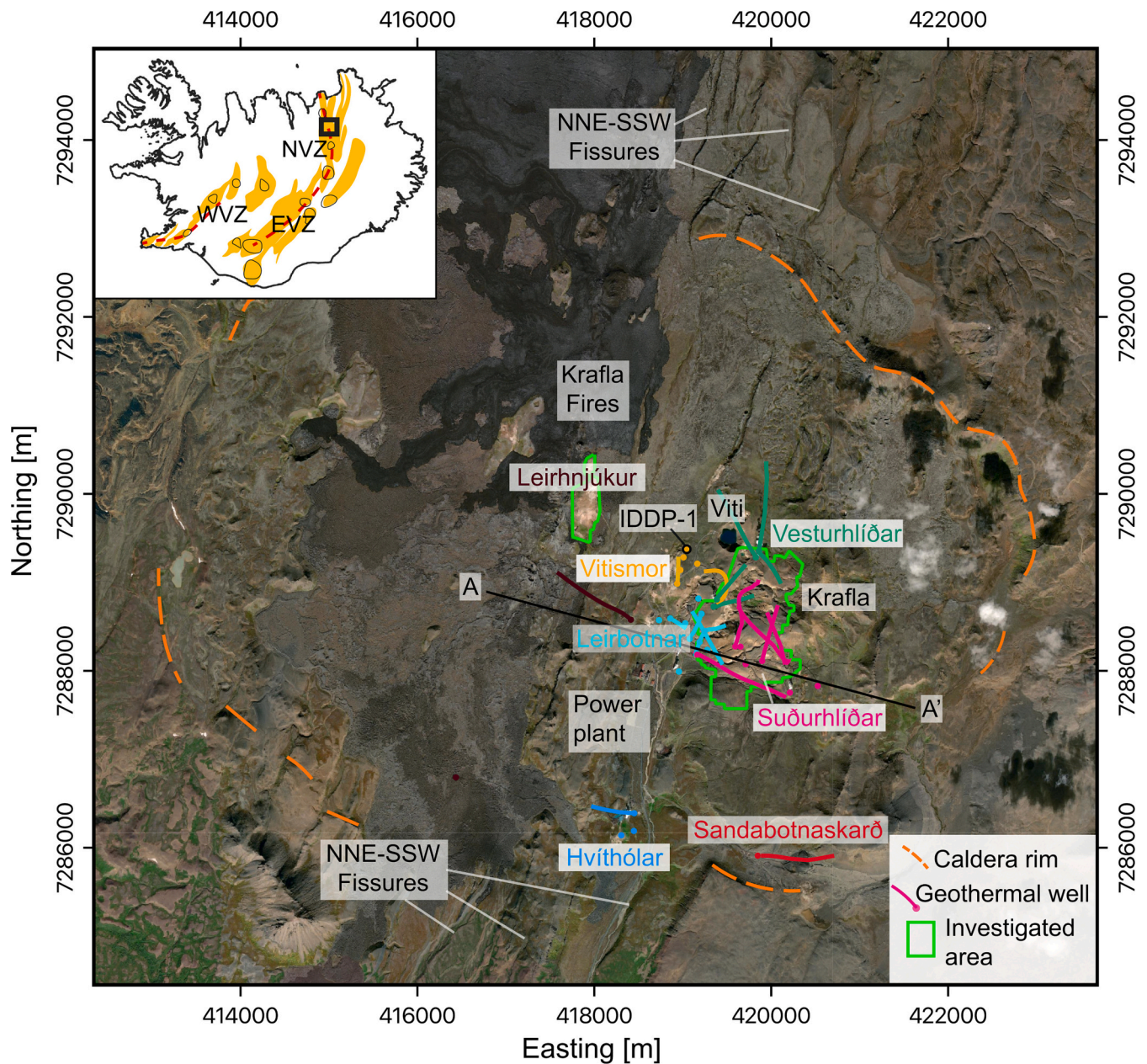
Fig. 1. Location of the Krafla geothermal field. The geothermal system developed in the 8–10 km-width caldera of Krafla (orange line), and is divided into 5 subfields: Leirbotnar (Vitismor included), Suðurhlíðar, Vesturhlíðar, Hvíthólar, and Sandabotnaskarð (Árnason, 2020; Scott et al., 2022). Soil CO$_2$ flux measurements were carried out over both the main production area of the geothermal field (Suðurhlíðar, Vesturhlíðar, and part of Leirbotnar) and Leirhnjúkur (green perimeter). The circles and lines reflect the geothermal well heads and subsurface paths (from Mortensen et al., 2015). The inset (modified after Árnason, 2020) shows the location of Krafla in the Northern Volcanic Zone (NVZ) of Iceland. WVZ and EVZ stands for Western and Eastern Volcanic Zone, respectively. The yellow areas reflect fissure swarms and the black contours are the main central volcanoes. Red dashed lines display spreading zones. Background is from ESRI imagery. Coordinates refer to the WGS 84/UTM zone 28 N. (For interpretation of the references to colour in this figure legend, the reader is referred to the web version of this article.)

were also erupted in the past. The last events of basaltic fissure eruptions occurred within the caldera around the Leirhnjúkur area (Fig. 1) in 1975–1984 and are often referred to as the Krafla Fires (Einarsson, 1991). Recent drilling of the KJ-39 and IDDP-1 geothermal wells encountered rhyolitic melts at shallow depth (~2 km; Elders et al., 2011; Mortensen et al., 2010), overlying the deeper mafic reservoir of the magmatic plumbing system. The similar petrological data of these rhyolites with those erupted in 1724, during the formation of the Viti maar (Montanaro et al., 2021; Fig. 1), suggest they extend throughout the center of the caldera (Rooyakkers et al., 2021).

Near the latest basaltic products of the Krafla Fires in Leirhnjúkur, the central part of the caldera hosts an active geothermal system with a predominant spatial extent over the western and southern flank of Mount Krafla (Fig. 1). Permeability appears to be higher in the upper first km of the caldera fillings, alternating hyaloclastite and lava flows, whereas decreases at greater depths in correspondence of intrusive crystalline bodies (Scott et al., 2022; Fig. 2). In general, permeability mainly developed along the fractures that follow the main tectonic direction of the fissure swarm, NNE-SSW, and the WNW-ESE alignment (Fig. 1), along which the latest geothermal wells were specifically drilled (e.g., KT-40, K-41; Mortensen et al., 2015). Depending on the relationship between these fractures, the meteoric recharge flow, and the stratigraphy of the Krafla caldera, the geothermal system can be divided into 5 subfields (Fig. 1; Árnason, 2020; Scott et al., 2022). Leirbotnar
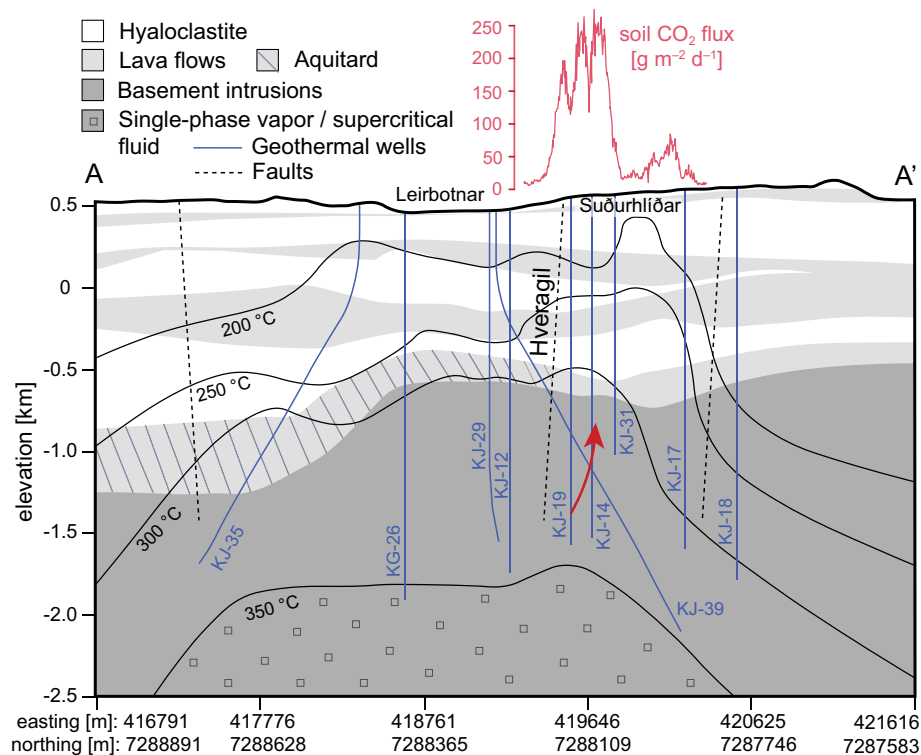
Fig. 2. Conceptual model of the Krafla geothermal system extending over the A-A' cross section in Figs. 1, 6, and soil CO_2 emission from Suðurhlíðar subfield extracted from Fig. 6a (modified after Scott et al., 2022). Isotherms (black curve) are derived from measured temperatures in geothermal wells (blue traces). The upflow of magmatic-hydrothermal fluids and the soil CO_2 emission (red curve) focus from the Hveragil fracture and Suðurhlíðar due to a low-permeability aquitard located at ~1 km depth in Leirbotnar. The two spikes in the soil CO_2 emission reflect the spatial distribution of the two WNW-ESE degassing structures cut by the A-A' line (Fig. 6a). The single-phase vapor or supercritical fluid region from which overlying boiling zones form through ascent and depressurization is also shown at the bottom of the model. Coordinates refer to the WGS 84/UTM zone 28 N. (For interpretation of the references to colour in this figure legend, the reader is referred to the web version of this article.)

(Vitismor included) is located to the west of the Hveragil fissure and is characterized by an isothermal zone extending in the first 1–1.5 km depth (e.g., IDDP-1 in Fig. 3). This sub-boiling zone is due to both a low permeability aquitard located along the lithological contrast between the caldera fillings and the intrusive bodies (Fig. 2), and the cooling effect of the NW-SE flow of meteoric water that preferentially recharges the system from the upper sequence of hyaloclastites and lava flows (Stefánsson, 1981; Darling and Ármannsson, 1989; Pope et al., 2016; Scott et al., 2022). Suðurhlíðar subfield is characterized by boiling conditions from the surface to ~2500 m depth (e.g., KJ-37 and KJ-39 in Fig. 3), reflecting one of the principal upflow zone of fluids not obstructed by the aquitard, which seems to interrupt after the Hveragil fracture (Pope et al., 2016; Scott et al., 2022; Fig. 2). Vesturhlíðar extends on the western flank of Mount Krafla and east of the Hveragil fissure (Fig. 1), showing boiling condition with depth, but also a shallow sub-boiling zone similar to Leirbotnar in some geothermal wells (e.g., KT-40 in Fig. 3; Gudmundsson and Mortensen, 2015; Mortensen et al., 2015). Hvíthólar is located in the southern part (Fig. 1) and appears to reflect the outflow zone of the hydrothermal fluid circulation, as suggested by the inversion of the temperature gradient with depth (Scott et al., 2022). Sandabotnaskarð is located to the south of Suðurhlíðar and east of Hvíthólar (Fig. 1). Despite the different thermal conditions in the first 1–1.5 km depth, the main production area shows common boiling zones and superheated/supercritical conditions at greater depth (Fig. 2), such as those tapped by wells KG-04, KG-25, KJ-36, KJ-39, IDDP-1 (Mortensen et al., 2015).

Evidence of degassing observed at the surface, such as fumaroles, boiling pools, and steaming grounds, suggest that the fluid upflow mostly occurs through the Suðurhlíðar, Vesturhlíðar, and Leirhnjúkur area. There, the diffuse emission of CO_2 from soils was measured

between 2004 and 2008 by Ármannsson et al. (2007) and Dereinda and Armannsson (2010). Ármannsson et al. (2007) carried out about 2559 measurements of the soil CO_2 flux with the accumulation chamber method over the entire Krafla caldera, but most of them covered a main area that included Suðurhlíðar and Vesturhlíðar subfields (1.1 km^2), and Leirhnjúkur area (0.2 km^2). The soil CO_2 emission from the main area accounted for about 22 t d^{-1}, while Leirhnjúkur soils degassed about 33 t d^{-1} of CO_2 (Ármannsson et al., 2007). Using clustering techniques (Sinclair, 1974; Chiodini et al., 1998), these authors grouped the soil CO_2 flux data into a normal hydrothermal population with mean ~ 115 g m^2 d^{-1}, a background at ~6 g m^2 d^{-1}, and a very low-flux population with a mean of ~1.6 g m^2 d^{-1} (Table 1). Later, Dereinda and Armannsson (2010) integrated the area investigated by Ármannsson et al. (2007) with new measurements carried out towards the north and west (~1 km^2), covering 2.5 km^2 with 3095 points. Due to the low fluxes measured from these new areas, the mean of the hydrothermal population calculated through clustering decreased to ~22.6 g m^2 d^{-1}, while the background and low-flux populations are comparable to those estimated by Ármannsson et al. (2007), that is ~6.8 and 0.4 g m^2 d^{-1} (Table 1) respectively. Soil CO_2 fluxes were later monitored through 406 and 360 measurements along the degassing lineaments revealed by the previous surveys in 2014 and 2017, respectively (Kristinsson et al., 2014, 2017). No clustered population of soil CO_2 fluxes were reported in 2014 and 2017, and due to the absence of measurements distributed over an areal extent, the CO_2 emission could not be calculated.
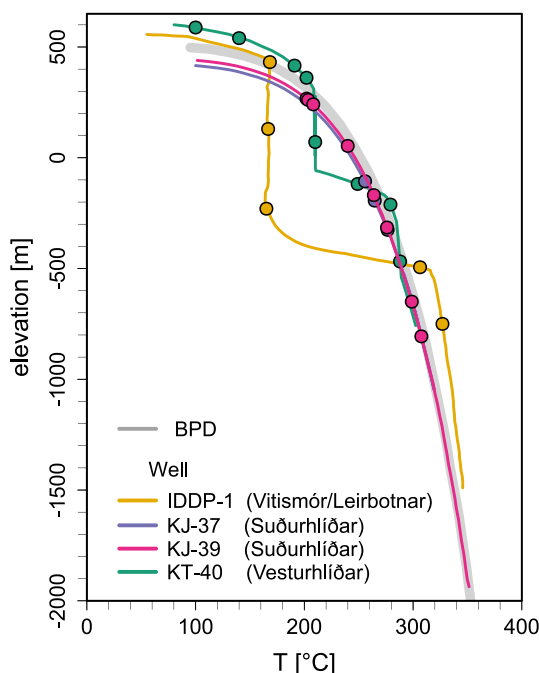
Fig. 3. Borehole temperature with depth (from Scott et al., 2022) and location of the calcite samples (circles) recovered from drill cuttings. The grey curve reflects the boiling point with depth curve (BPD), assuming an elevation of 500 m. KJ-37 and KJ-39 were drilled in the Suðurhlíðar geothermal subfield, which is characterized by boiling conditions from the surface to downhole depths >2000 m. KT-40 shows a sub-boiling zone characterized by isothermal conditions, and then a step increase towards the BPD, likely due to shallow cold water recharge inflow in the Vesturhlíðar subfield. IDDP-1 shows a more extended isothermal condition, which characterizes the Leirbotnar subfield, reflecting the effect of the water recharge and the presence of an aquitard between shallower hyaloclastites and lavas (~1 km) and deeper basement intrusions.

Table 1
Normal populations of the soil CO_2 fluxes in 2022 (this study; *section 3.2*) compared to those estimated between 2004 and 2008 by Ármannsson et al. (2007) and Dereinda and Ármannsson (2010).

Ármannsson et al. (2007): main production area			Dereinda and Ármannsson (2010): main production area		
Source	f [%]	Mean soil CO_2 flux [g m^{-2} d^{-1}]	Source	f [%]	Mean soil CO_2 flux [g m^{-2} d^{-1}]
Background	10	1.6	Background	3.5	0.39
Background	80	6	Background	71.5	6.81
Hydrothermal	10	115	Hydrothermal	25	22.6

This study: main production area			This study: Leirhnjúkur		
Source	f [%]	Mean soil CO_2 flux [g m^{-2} d^{-1}]	Source	f [%]	Mean soil CO_2 flux [g m^{-2} d^{-1}]
Background	55	4.3 ± 0.3	Background	49	4.9 ± 0.5
Intermediate	41	30.5 ± 2.3	Hydrothermal	51	117.7 ± 35.1
Hydrothermal	4	1641 ± 614			

3. Material and methods

3.1. Soil temperature and CO_2 emission

Measurements of the soil CO_2 emission and temperature were carried out over the main production area (561 measurements over 1.43 km^2), including Suðurhlíðar, Vesturhlíðar, and partly Leirbotnar geothermal subfields, and at Leirhnjúkur (123 measurements over 0.19 km^2; Fig. 1). We chose these locations according to both field observation and previous CO_2 flux campaigns available in the literature (Ármannsson et al., 2007; Dereinda and Armannsson, 2010), adopting a regular sample grid of 50 × 50 m. A detail at 25 × 25 m was also carried out over Leirhnjúkur. Due to variable meteorological conditions, the measurements were performed from 19 to 23 June 2022 in the main area, and 1–2 July 2022 in Leirhnjúkur, thus avoiding strong episodes of rain and winds. To measure the CO_2 flux (g m^{-2} d^{-1}) from the soil, we used two portable flux meters constructed by the West Systems (type A and B chambers) based on the accumulation chamber method (Chiodini et al., 1998), which briefly consists in measuring the increase of the CO_2 concentration over time in a cylindrical chamber placed on the soil (Fig. 4). The gas flows from the chamber to an infrared sensor (LI-COR Li-820), and then is reinjected into the chamber to avoid depressurization (Fig. 4). The temporal increase in CO_2 revealed by the infrared sensor is proportional to the CO_2 flux from the soil and is visualized in real-time on a smartphone (Fig. 4). Both portable flux meters were calibrated in the West Systems laboratory before their usage at Krafla. To measure the soil temperature, we inserted a k-type thermocouple at 15 cm depth.
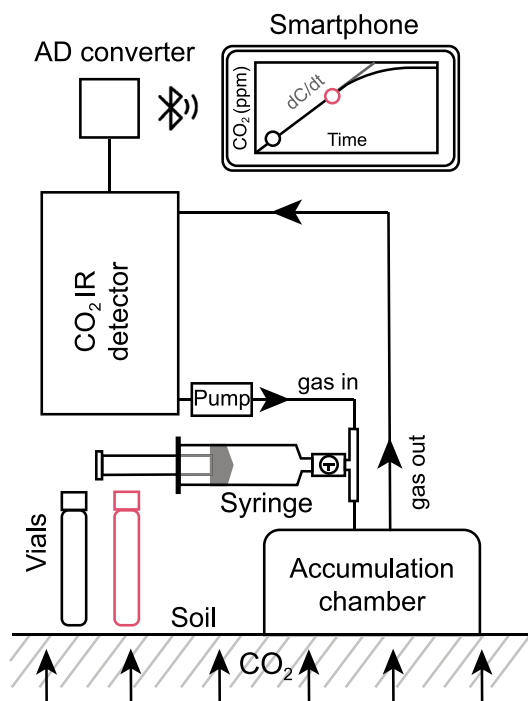

Fig. 4. Scheme of the fluxmeter coupled with a gas sampling apparatus for the measurement of the soil CO_2 emission and analysis of the C isotopes of the CO_2 efflux (modified after Chiodini et al., 2008). After the accumulation chamber is placed over the soil, the gas is pumped through an infrared (IR) detector and is reinjected into the chamber. The concentration of the CO_2 within the chamber measured by the IR detector is transmitted in real-time to a smartphone and increases over time. The slope (dC/dt) of such increase is proportional to the soil CO_2 flux. For the analysis of the $\delta^{13}C$ of the CO_2 efflux, two gas samples are sampled from the tubing of the AC circuit through a T-connector and a syringe, and stored in glass vials. The first sample is collected at the beginning of the flux measurement (low CO_2 concentration; black), and the second one after a few minutes (high CO_2 concentration; red). The $\delta^{13}C_{CO_2}$ is then graphically determined in Fig. 7 (*section 3.3*). (For interpretation of the references to colour in this figure legend, the reader is referred to the web version of this article.)

3.2. Statistical modeling of spatial data

3.2.1. Clustering subgroups of soil CO_2 flux and T data

The gas emitted into the atmosphere from soil covering magmatic-hydrothermal systems generally reflect both biogenic and hydrothermal sources, often resulting in a bimodal distribution of the data (e.g., Fig. 5a). The mean and standard deviation of each normal population can be estimated using clustering techniques visualized on histograms, probability plots (Sinclair, 1974, 1991; Chiodini et al., 1998) or Q-Q plots (Benaglia et al., 2009). The Q-Q plot shows the sample quantiles against the theoretical quantiles of a normal distribution with mean 0 and variance 1. In this plot, *n* normal populations distribute along straight lines, and their mixing results in a curve with *n-1* inflection points. To estimate the mean, standard deviation, and fraction of each
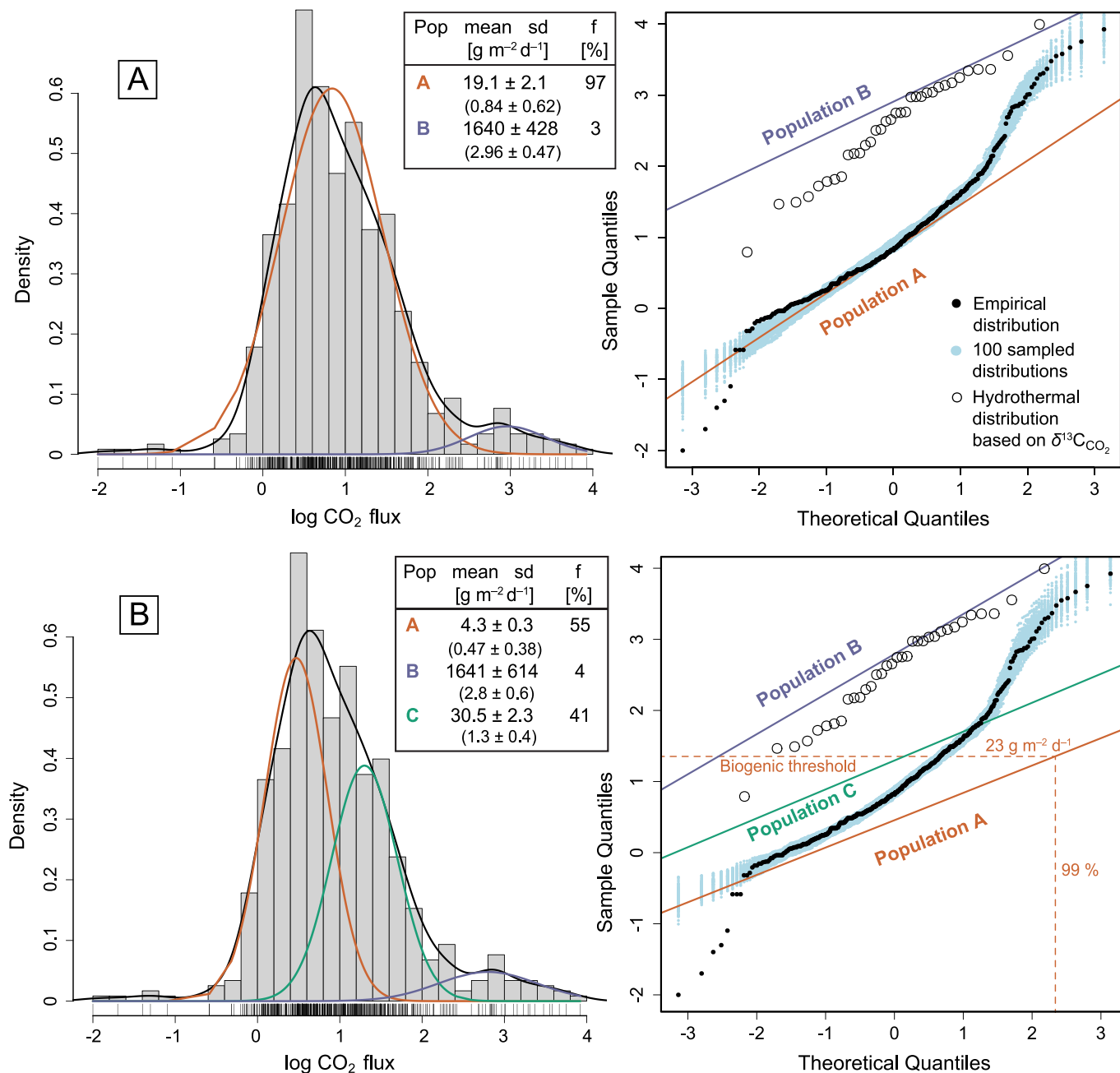

Fig. 5. Density plot (left) and Q-Q plot (right) of the logarithm of the soil CO_2 fluxes (g m^{-2} d^{-1}) from the main area, modeled through 2 (a) and 3 (b) lognormal populations. (a) The distribution of the data (black curve and circles) is modeled with the overlap of 2 lognormal populations (A and B) by an EM algorithm (*section 3.2.1*). A small fraction (f) of the data reflects a high-CO_2 flux population (B, purple curve), while most of them (97%) are controlled by a lower CO_2-flux population (A, orange curve). (b) The distribution of the data is modeled by three lognormal population, showing the same control of the high-CO_2 flux population (B) on a small fraction of the data. The remaining part of the distribution is clustered in a low-CO_2 flux population (A), and an intermediate-flux population (C). This low-CO_2 flux population (A) reflects the soil biologic activity, and its 99th percentile (23 g m^{-2} d^{-1}) is taken as the threshold above which soil CO_2 emissions are considered nonbiogenic. This threshold enables us to spatially constrain the degassing of hydrothermal CO_2 (see white contours in Fig. 6). The light blue circles in the Q-Q plot are 100 distributions sampled from the modeled A-B (a) or A-B-C (b) mixing distribution. The white circles are the CO_2 fluxes correspondent to the magmatic-hydrothermal population of data, clustered on the basis of the C isotopes of the CO_2 emission (*section 3.3*; Fig. 7b). Most of these overlap the population B, although a very few of them might overlaps with population C. (For interpretation of the references to colour in this figure legend, the reader is referred to the web version of this article.)

population contributing to the whole distribution, we used the 'normalmixEM' function of the 'mixtools' (Benaglia et al., 2009) package for R (R Core Team, 2023). This function uses an expectation-maximization (EM) algorithm for iteratively finding maximum likelihood estimates of the parameters (mean, standard deviation, and fraction) of each normal distribution. The advantage of using an EM algorithm is the unsupervised clustering of the normal populations, meaning that the function automatically fit the distribution. On the contrary, the graphical approach of Sinclair (1974) needs the parameters to be specified and therefore is affected by a greater degree of subjectivity. If the modeled distributions are lognormal, as in the case of the CO_2 flux data (Fig. 5), their mean and standard deviation (in $g\,m^{-2}\,d^{-1}$) is then estimated using a Monte Carlo simulation.

3.2.2. Sequential Gaussian simulation (sGs)

To estimate the total CO_2 emission and the spatial distribution of the hydrothermal fluid upflow zones over the monitored areas, we need to simulate the CO_2 flux over the unsampled locations of the grid using sequential Gaussian simulations (sGs; e.g., Cardellini et al., 2003). First, the data are transformed to a normal distribution with mean 0 and variance 1 (nscores), and used to model the spatial continuity of the CO_2 flux over the grid through the variogram (Fig. S1). Once the variogram model is calculated, the CO_2 flux is estimated at each node of the grid (5 × 5 m) through sGs. Here, nearby data and previously simulated data are used to construct the conditional distribution by kriging, from which the simulated value is drawn and assigned to the grid node. This procedure continues following a random path through the grid nodes until all of these contain simulated values, thus completing one realization. For both the main area and Leirhnjúkur, we constructed 1000 realizations, back-transformed the data from the "normal space" to continuous variables, and averaged the results in the center of each 5 × 5 m cell. This enabled us to construct soil CO_2 flux and T maps (Fig. 6).

This statistical procedure was performed using the 'gstat' (Pebesma, 2004) package for R (R Core Team, 2023), following similar exploratory data analyses performed with GSLIB (Deutsch and Journel, 1998; Cardellini et al., 2003). In particular, the variogram model is calculated with the 'fit.variogram' function, which iteratively finds the best fit through weighted least squares (Pebesma, 2004). This is a big advantage with respect to the visual fitting, which is manually performed by the user, and is thus affected by a degree of subjectivity. The conditional simulations were performed using the 'krige' function.

3.3. Carbon isotope of the soil CO_2 emission

To define the C isotope composition of the soil CO_2 efflux, we used a methodology described in Chiodini et al. (2008) and Bini et al. (2020), based on the sampling of the gas circulating within the accumulation chamber. We inserted a T-connector with a pierceable septum at the gas input of the flux meter for enabling gas sampling with a syringe (Fig. 4), and we carried out further 88 flux measurements over both the main area ($n = 81$) and Leirhnjúkur ($n = 7$). A few measurements over Suðurhlíðar were carried out outside the regular grid, in correspondence with altered argillic soils with dispersed fumarolic activity. During each CO_2 flux measurement, we sampled the gas at the beginning (sample I; black circle in Fig. 4), when the CO_2 concentration within the chamber was relatively low and predominantly atmospheric, and at the end, after the CO_2 concentration has increased (sample II; red circle in Fig. 4). The two gas samples were then stored in 12-ml Labco Exetainer glass vials (Fig. 4) and analyzed in the laboratory of INGV Napoli, Osservatorio Vesuviano, within a week from the sampling. The C isotope contents (in ‰ versus PDB) in the gas vials were determined using a continuous flow isotope mass ratio spectrometer (Thermo-Finningan Delta XP, He as carrier), connected to the Gasbench II, equipped with an autosampler ($\delta^{13}C_{CO2}$ standard error ± 0.1‰). Each couple of gas samples (I and II) plotted in the $\delta^{13}C_{CO2}$–$1/CO_2$ space reflects a binary mixture (straight line) between a low- and a high-concentration CO_2 endmember

(Fig. 7a). Therefore, the extrapolation of $\delta^{13}C_{CO2}$ at $1/CO_2 = 0$ from each linear regression model enables us to estimate the $\delta^{13}C_{CO2}$ of the high-CO_2 (i.e., pure CO_2) endmember. These extrapolated $\delta^{13}C_{CO2}$ are then treated with unsupervised clustering (*section 3.2.1*) for defining the $\delta^{13}C_{CO2}$ of the hydrothermal and biogenic gas sources (Fig. 7b).

3.4. Carbon and oxygen isotopes of hydrothermal calcite and water

Carbon and oxygen isotopes were also determined on 24 samples of calcite rock cuttings recovered at specific depths during the drilling of wells KJ-37, KJ-39, KT-40, and IDDP-1 (Fig. 3). Calcite samples were hand-picked under optical microscopy, reduced to a fine powder using an agata mortar, and stored in 12-ml Labco Exetainer vials (1–5 g). C and O isotopes of these calcite samples were then analyzed with the same instrumental apparatus used for $\delta^{13}C_{CO2}$ determination (*section 3.3*). The vials were flushed with He and partly filled with drops of H_3PO_4 to react with calcite and release CO_2, which is then analyzed for $\delta^{13}C_{CaCO3}$ (in ‰ versus PDB) and $\delta^{18}O_{CaCO3}$ (in ‰ versus VSMOW) through mass spectrometry.

Assuming that calcite precipitated through boiling and was in isotopic equilibrium with the hydrothermal fluid, $\delta^{13}C_{CaCO3}$, $\delta^{18}O_{CaCO3}$, and formation temperatures can be used in the relevant fractionation factor dependencies with T to recalculate the C and O isotope of the hydrothermal fluid (e.g., Simmons and Christenson, 1994). In particular, the $\delta^{18}O_{H2O}$ can be calculated according to the temperature-dependent O isotopic exchange between the fluid and calcite (T in K) expressed by Friedman and O'Neil (1977).

$$\delta^{18}O_{H_2O} = \delta^{18}O_{CaCO3} - 2.78 \times 10^6/T^2 + 2.89, \tag{1}$$

whereas the $\delta^{13}C_{CO2}$ is calculated using the CO_2-$CaCO_3$ isotope fractionation factor determined by Bottinga (1968) for temperature between 0 and 550 °C.

$$\delta^{13}C_{CO_2} = \delta^{13}C_{CaCO3} - 2.9880 \times 10^6/T^2 + 7.6663 \times 10^3/T - 2.4612. \tag{2}$$

3.5. Mass and thermal flow of the geothermal system

The thermal energy of geothermal systems dominated by convection, boiling, and steam separation can be estimated using the soil CO_2 gas emission and the CO_2 concentrations in both liquid and vapor phases circulating in the subsurface (Chiodini et al., 2007, 2021; Bini et al., 2019). When hydrothermal liquids boil, they generate a vapor phase that contains steam, CO_2, and other non-condensable gases; the vapor ascends and then condenses as it approaches the surface (Fig. 8). Condensation of water in the shallow subsurface heats the soil, while the low-solubility CO_2 escapes into the atmosphere (Fig. 8). The CO_2 emission can be used with the H_2O/CO_2 weight ratio of dry steams (e.g., fumaroles or dry vapor from boreholes) to calculate the mass flow rate of the condensed vapor

$$\dot{m}_{H_2O,cond} = \dot{m}_{CO_2} \times \left(\frac{C_{H_2O}}{C_{CO_2}}\right)_V \tag{3}$$

where $\dot{m}_{H_2O,cond}$ is the mass flow rate of the condensed steam in $kg\,s^{-1}$, $\dot{m}_{CO_2}$ is the soil CO_2 emission in $kg\,s^{-1}$, and $\left(\frac{C_{H_2O}}{C_{CO_2}}\right)_V$ is the weight ratio of H_2O and CO_2 (in $mg\,kg^{-1}$) in the dry steam. The energy release through subsurface vapor condensation is computed through

$$\dot{E}_{H_2O,cond} = \dot{m}_{H_2O,cond} \times \left(h_{V,T_b} - h_{L,T_b} + h_{L,T_b} - h_{L,T_a}\right) \times 10^{-3} \tag{4}$$

where $\dot{E}_{H_2O,cond}$ is the thermal energy flow rate due to steam condensation in MW, h_{V,T_b} and h_{L,T_b} are the specific enthalpy of vapor and liquid H_2O at the boiling temperature (2673 and 411.6 $kJ\,kg^{-1}$, respectively, at 98.2 °C, corresponding to an elevation of 550 m), and h_{L,T_a} is the specific enthalpy of liquid water at ambient temperature (42.02 $kJ\,kg^{-1}$ at
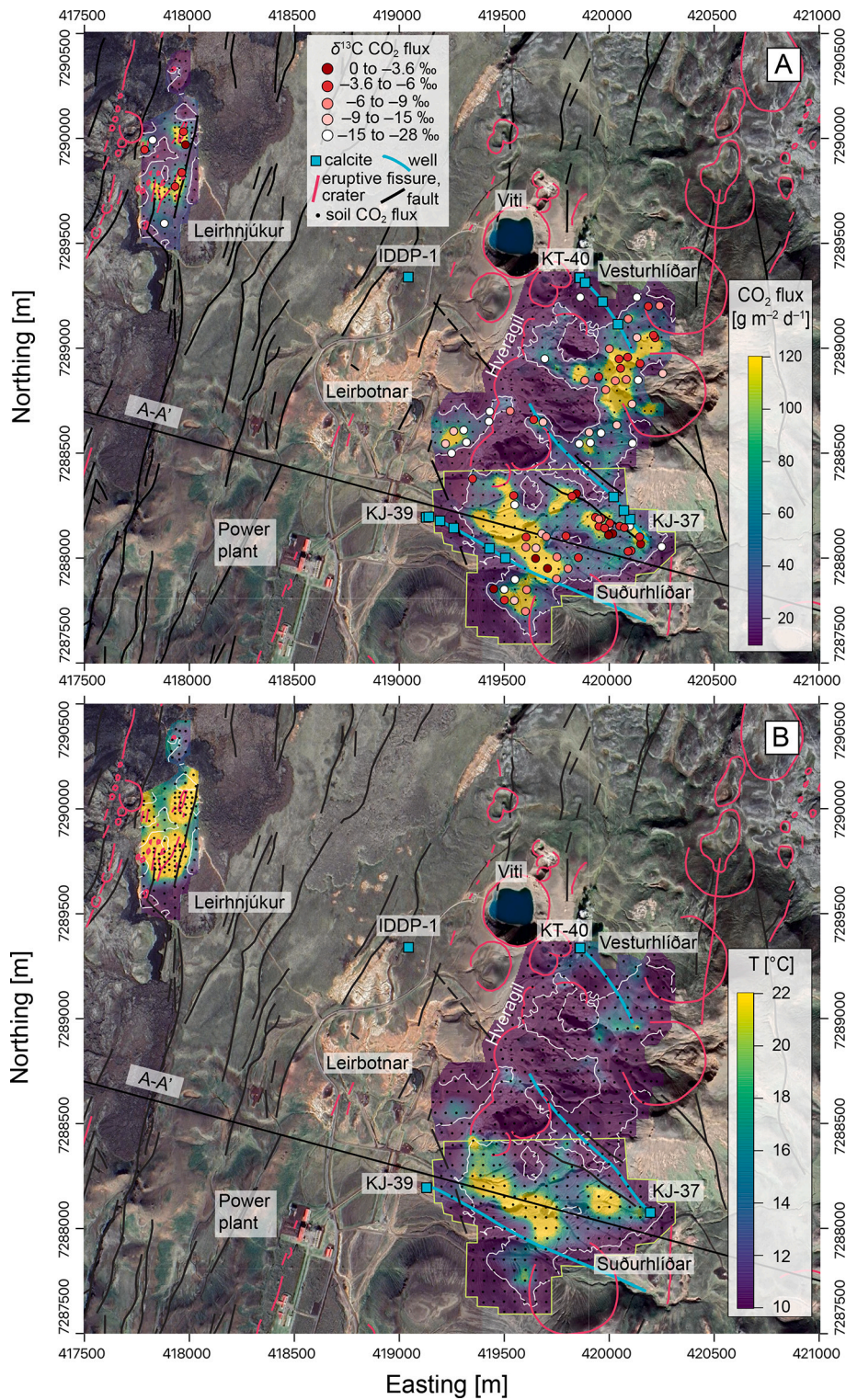
Fig. 6. Soil CO_2 flux (a) and T maps (b) of the main area and Leirhnjúkur constructed by averaging the results of 1000 sGs over 5 × 5 m grids. The soil CO_2 emission occurs from three diffuse degassing structures (DDS) in the main area, extending over Vesturhlíðar (N), Suðurhlíðar (S), and part of Leirbotnar (W) subfields, and one in Leirhnjúkur (white contour). These DDS are spatially constrained by the soil CO_2 flux biogenic threshold of 23 g m^{-2} d^{-1} (white contour), corresponding to the 99th percentile of the population A in Fig. 5b. Both CO_2 emission and T of these DDS are predominantly controlled by the fissure direction (NNE-SSW) and a WNW-ESE trend, and are spatially correlated. The best CO_2 flux-T correlation is in Suðurhlíðar and Leirhnjúkur. Soil CO_2 flux measurements are displayed as black circles. Locations of the gas collected from the accumulation chamber (Fig. 4) and the correspondent $\delta^{13}C$ of the CO_2 emission (extrapolated values from Fig. 7a; *section 3.3*) are also shown as circles colored with a gradient from red to white (as $\delta^{13}C_{CO2}$ decrease). Calcite samples recovered at increasing well depths for the determination of their $\delta^{13}C$ and $\delta^{18}O$ are shown as cyan squares. Eruptive fissures and explosion craters (red line), faults (black line; from Sæmundsson, 2008), well paths in the subsurface (cyan line; from Mortensen et al., 2015), and A-A' section (from Scott et al., 2022; see also Fig. 2) are also shown for comparison. Background is from Google satellite imagery. Coordinates refer to the WGS 84/UTM zone 28 N. (For interpretation of the references to colour in this figure legend, the reader is referred to the web version of this article.)
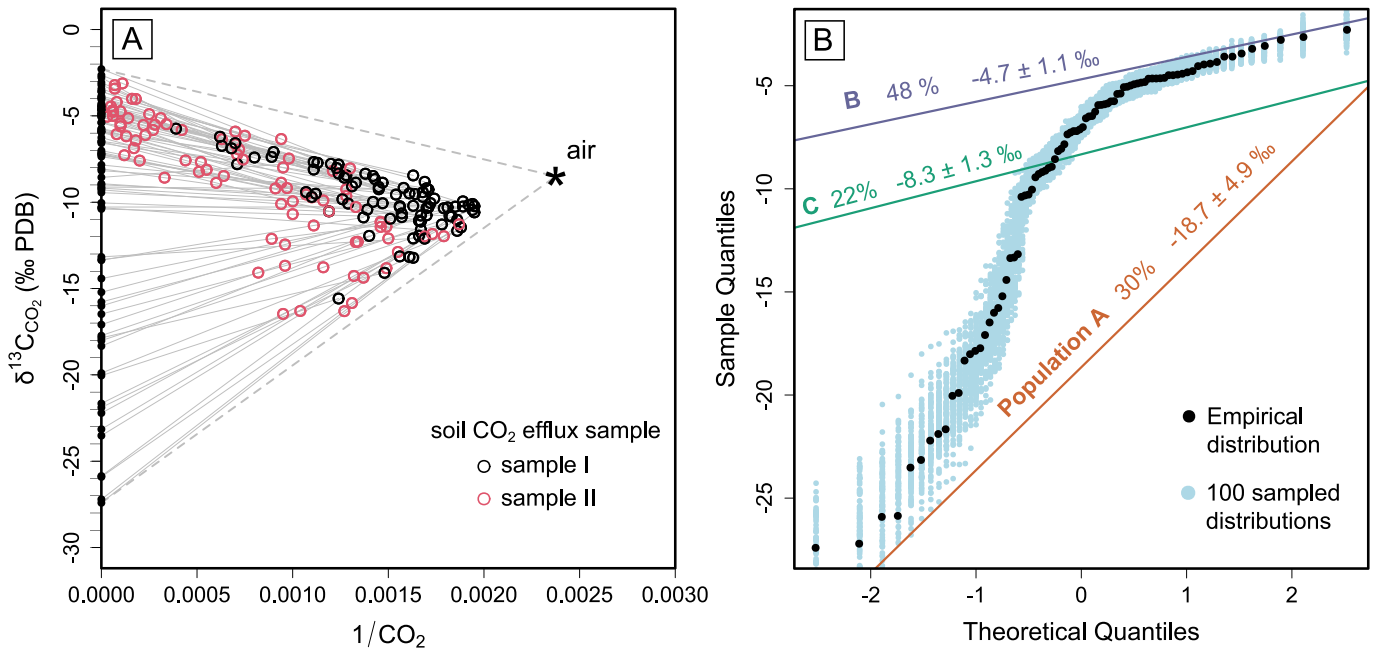
Fig. 7. (a) Carbon isotopes of the CO_2 efflux plotted against the inverse of the CO_2 concentration (ppm) and (b) Q-Q plot of the $\delta^{13}C_{CO2}$ extrapolated at $1/CO_2 = 0$. The black and red circles (7a) display the sample of the CO_2 efflux collected at the beginning (sample I; low CO_2 concentration) and at the end (sample II; high CO_2 concentration) of the measurement (see Fig. 4), respectively. The grey lines are linear regressions through each couple of samples (sample I and II) collected during each soil CO_2 flux measurement, reflecting binary mixing between air and a higher-CO_2 concentration endmember. The intercept returns the $\delta^{13}C$ of the gas source entering the accumulation chamber. The gas distributes along two predominant trends, suggesting the occurrence of two endmembers with $\delta^{13}C_{CO2}$ of ~ -5 and -25 ‰. Unsupervised clustering of the extrapolated values reveals that the two endmembers have $\delta^{13}C_{CO2}$ of $\sim -4.7 \pm 1.1$ ‰ and -18.7 ± 4.9 ‰, respectively. The former approaches the carbon isotopes of the fumarole (from -2.4 to -4.8 ‰; Barry et al., 2014) and borehole gases (-3.3 ± 1.1 ‰; Ármannsson, 1998; Barry et al., 2014; Beaudry et al., 2021), the latter that of the soil biological processes. (For interpretation of the references to colour in this figure legend, the reader is referred to the web version of this article.)

10 °C). The energy release through condensation accounts for both the latent heat of condensation and the cooling of the condensed vapor to ambient temperature.

Assuming that all the CO_2 emitted into the atmosphere from soils was previously dissolved into the hydrothermal liquid, and separated through boiling (Fig. 8), we can calculate the mass and thermal flow rate of the liquid in the subsurface, through

$$\dot{m}_{H_2O} = \dot{n}_{CO_2} \Big/ m_{CO_2} \qquad (5)$$

and

$$\dot{E}_{H_2O} = \dot{m}_{H_2O} \times h \times 10^{-3} \qquad (6)$$

where $\dot{m}_{H_2O}$ is the mass flow rate in kg s^{-1}, $\dot{n}_{CO_2}$ is the soil CO_2 emission in mol s^{-1}, m_{CO_2} is the molality of CO_2 in the liquid in mol kg^{-1}, and $\dot{E}_{H_2O}$ is the thermal energy flow rate of the liquid in MW. Since the boiling zones of Krafla are thought to form through depressurization of supercritical fluids located in the deep root of the hydrothermal system (Fig. 8; Heřmanská et al., 2019; Scott et al., 2022), Eqs. (5 and 6) can be used to calculate the energy and mass flow of these deep fluids by knowing their molality and enthalpy.

Due to the assumptions of the model, mass and thermal flow estimates based on the soil CO_2 emission can have large uncertainties. For example, if part of the soil CO_2 emission was not dissolved in the original liquid, we might overestimate these flows. In contrast, if ascending CO_2 partly dissolves in shallow groundwater, both the soil CO_2 emission and the water and heat flows will be underestimated. However, the uncertainty of these estimates can be reduced by applying this method to those areas where CO_2 is emitted from hot soils (close to the water-boiling temperature), that is where condensation of the ascending vapors occurs at a few meters depth. In these cases, the removal of CO_2 in

shallow groundwater is negligible and the method provides a plausible order of magnitude of both mass and thermal flows.

4. Results

4.1. CO_2 emission from Krafla soils

4.1.1. Main area (Suðurhlíðar-Vesturhlíðar-Leirbotnar)

The soil CO_2 flux measurements carried out over the main production area of the Krafla geothermal field (561 points over 1.43 km^2) span the range from 0.01 to 5632 g m^{-2} d^{-1}, extending over a regular grid of 50×50 m (Fig. 6a). Their distribution reflects the overlap of two populations (Fig. 5a), suggesting a CO_2 contribution from two separate sources. The population A (orange curve) predominantly controls (97%) the density distribution (black curve), showing CO_2 flux of 19.1 ± 2.1 g m^{-2} d^{-1}, while the population B (purple curve) only accounts for the 3% of the data but shows a significant CO_2 flux of 1640 ± 428 g m^{-2} d^{-1} (Fig. 5a). This bimodality is also in good agreement with the general soil T distribution, which is predominantly controlled ($\sim$90%) by a normal population with 9.6 ± 0.1 °C, and for a very small fraction by T close to that of water boiling ($\sim$96 °C). Notably, the usage of a third normal population for modeling the soil CO_2 fluxes improves the goodness of fit particularly over the low values of the density distribution (Fig. 5b), potentially revealing the most likely background distribution (A = 4.3 ± 0.3 g m^{-2} d^{-1}; 55% of the data). In this three-distribution-model, a small fraction of the data is controlled by the same high-flux population of the two-distribution-model (B), whereas the 41% reflects intermediate soil CO_2 fluxes (C = 30.5 ± 2.3 g m^{-2} d^{-1}; Fig. 5b; Table 1). We used the 99th percentile of this background population (23 g m^{-2} d^{-1}; Fig. 5b) as the biologic threshold above which soil CO_2 fluxes are considered nonbiogenic. This enables us to spatially constrain the main diffuse degassing structures (DDS) of magmatic-hydrothermal CO_2.
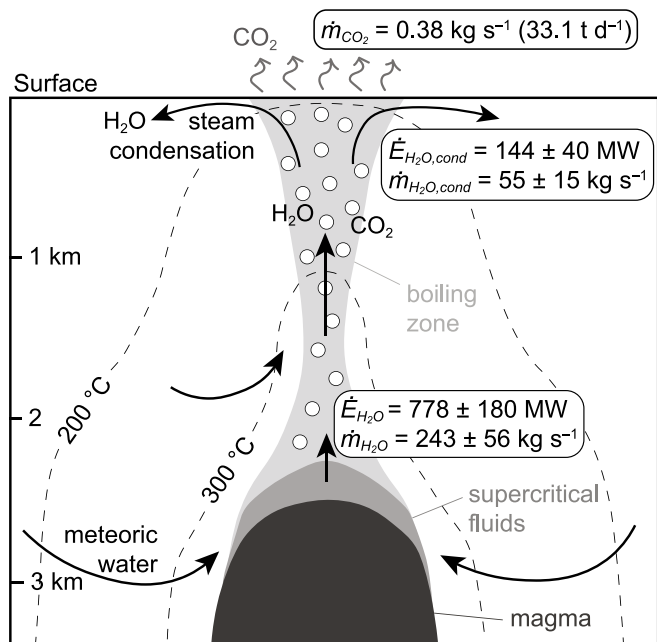
Fig. 8. Conceptual model of the hydrothermal fluid flow feeding the soil CO_2 emission in the Suðurhlíðar subfield (modified after Heřmanská et al., 2019). Supercritical fluids form in the vicinity of a shallow intrusion due to conductive heating of meteoric water, and their upflow and depressurization generates a vapor-liquid zone extending up to the surface (Heřmanská et al., 2019; Scott et al., 2022). Vapors and CO_2 separated through boiling condenses as they approach the surface, releasing thermal energy. The low-soluble CO_2 diffuses through the soil and is emitted into the atmosphere. The mass and energy flow rate of both supercritical fluids and condensed steam are calculated through Eqs. (3–6).

The spatial distribution of the soil CO_2 emission, modeled with sGs using an exponential variogram model (Fig. S1), is grouped in three main DDS, extending over Vesturhlíðar (N), Suðurhlíðar (S), and part of Leirbotnar (W) subfields (Fig. 6a; white contour). The diffuse degassing of CO_2 from these DDS spatially correlates with both the predominant NNE-SSW and secondary WNW-ESE fault directions cutting the geothermal system (Fig. 6a; black line). In particular, the Vesturhlíðar DDS is mostly controlled by the NNE-SSW direction, showing one evident anomaly where well drilling recently focused (KT-40, K-41; Gudmundsson and Mortensen, 2015), and a weaker emission close to the Hveragil eruptive fissure (Fig. 6a). The Suðurhlíðar DDS is characterized by two distinct WNW-ESE lineaments of CO_2 emissions (Fig. 6a, 2), which might be cut by the continuation of the NNE-SSW-trending emission of Vesturhlíðar (Fig. 6a). This spatial continuity of such anomaly is also suggested by the soil T map (Fig. 6b), which correlates with the whole spatial distribution of the CO_2 emission. Notably, the Vesturhlíðar DDS is characterized by a somewhat lower T than that of Suðurhlíðar DDS, which in contrast records very high T (close to water-boiling T) in correspondence with the two WNW-ESE CO_2 anomalies (Fig. 6b).

The entire emission of CO_2 from the main area computed by averaging 1000 realizations (5×5 m) constructed with sGs (*section 3.2.2*) accounts for 68.7 ± 6.5 t d^{-1}, including both magmatic-hydrothermal and biogenic CO_2 sources. Assuming that the population A of the three-distribution-model (~ 4.3 g m^{-2} d^{-1}; Fig. 5a) derives from the soil biological activity, by multiplication by the areal extent (1,431,250 m^2) we can estimate the background soil CO_2 emission at 6.2 t d^{-1}. Hence, the magmatic-hydrothermal CO_2 emitted into the atmosphere is about 62.5 ± 6.5 t d^{-1}.

4.1.2. Leirhnjúkur

The distribution of the soil CO_2 emission from the Leirhnjúkur area (123 points over 187,600 m^2) varies from 0.9 to 1287.4 g m^{-2} d^{-1} and is explained for the 49% by a background population with mean and standard deviation of 4.9 ± 0.5 g m^{-2} d^{-1} and for the remaining 51% by a hydrothermal population of 117.7 ± 35.1 g m^{-2} d^{-1} (Fig. 9a; Table 1). This bimodality correlates with the soil T, whose distribution reflects the mixing of a 11.2 ± 0.3 °C population (43%) with a 36.5 ± 2.9 °C population (57%; Fig. 9b). It is worth noting that the low-CO_2-flux population (A) is practically the same of the main area, thus suggesting that ~ 4.3 g m^{-2} d^{-1} is a reasonable value for the background CO_2 emission at Krafla. On the other hand, the high- CO_2-flux population of the two areas differ by one order of magnitude (Table 1).

The emission of hydrothermal CO_2 from the Leirhnjúkur area modeled with sGs appears to follow the predominant fissure-swarm direction, in proximity of the Krafla Fires eruptive fissure (Fig. 1, 6a). This high-permeability zone is also highlighted by the soil T, which is spatially correlated to the soil CO_2 flux and even larger in extent. The total soil CO_2 emission calculated with sGs, using spherical variogram models to explain the spatial continuity of the data (Fig. S2), accounts for 7.9 ± 0.9 t d^{-1}. Considering the same CO_2 background value for the entire Krafla area, that is 4.3 g m^{-2} d^{-1} (population A, main area; Fig. 5b), the magmatic-hydrothermal CO_2 emitted into the atmosphere would account for about 7.1 t d^{-1}.

4.2. Carbon and oxygen isotopes of CO_2 and $CaCO_3$ reveal the sources of Krafla fluids

The soil CO_2 gas samples (88×2) collected within the accumulation chamber (Fig. 4; Table S1) reflect mixtures between air and two high-CO_2-concentration endmembers with very different carbon isotopes, approximately pointing to $\delta^{13}C_{CO2} \sim -5$ and -25 ‰ (versus PDB), respectively (Fig. 7a). More specifically, unsupervised clustering of the computed $\delta^{13}C$ of the CO_2 efflux (extrapolated at $1/CO_2 = 0$; *section 3.3*) returns a distribution with $\delta^{13}C_{CO2} = -4.7 \pm 1.1$ ‰ (Fig. 7b), which accounts for the half of the data and approaches the C isotope composition of borehole (-3.3 ± 1.1 ‰; Ármannsson, 1998; Barry et al., 2014; Beaudry et al., 2021) and fumarole gases (from -2.4 to -4.8 ‰; Barry et al., 2014). The other predominant endmember most likely reflects the background CO_2, being $\delta^{13}C_{CO2}$ very negative (-18.7 ± 4.9 ‰) and in the range of biological C production (Fig. 7b). Notably, the CO_2 fluxes correspondent to the $\delta^{13}C_{CO2}$ of the population B (Fig. 7b) overlap with those of the analogous population in Fig. 5, although a very few of these show lower values that might also overlap with population C (Fig. 5).

The isotope composition of the hydrothermal fluids in equilibrium with calcite samples show a somewhat increasing $\delta^{13}C_{CO2}$ and $\delta^{18}O_{H2O}$ values with depth (Table 2; Fig. 10). The $\delta^{18}O_{H2O}$ values display a predominant contribution from the $\delta^{18}O_{H2O}$ of the local meteoric water recharge (-12.5 ‰; Sveinbjornsdottir et al., 1986; Darling and Ármannsson, 1989). A few of them overlap the $\delta^{18}O_{H2O}$ of the deep geothermal liquid reservoir (-10.7 ± 0.9 ‰; Pope et al., 2016; Ricci et al., 2022), while at shallower depth they show more negative values (Fig. 10a). These data are overall in good agreement with those estimated using epidote samples (Fig. 10a) from Pope et al. (2016), which are stable at greater temperature-depth with respect to carbonates. However, calcites appear to record more magmatic condition at shallower depths with respect to these epidote samples (Fig. 10). The average carbon isotopes of the CO_2 of the hydrothermal fluids from which calcite precipitated (-2.8 ± 1.2 ‰) is very similar to both that of the borehole and fumarole fluids (-3.3 ± 1.1 ‰; Ármannsson, 1998; Barry et al., 2014; Beaudry et al., 2021), and that of the Icelandic mantle (-2.5 ± 1.1 ‰; Fig. 10b), estimated by Barry et al. (2014) through subglacial basaltic glasses. Notably, the deepest samples appear to record more magmatic conditions (Fig. 10b).

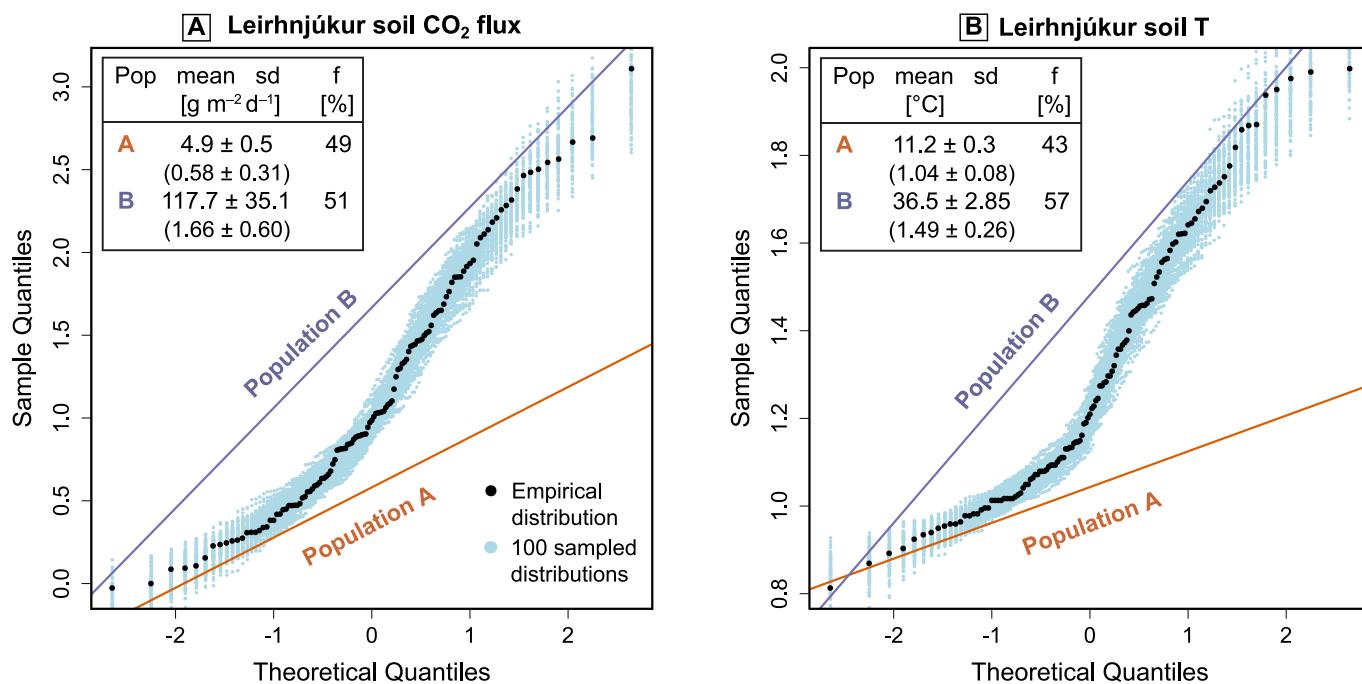**Fig. 9.** Q-Q plot of the logarithm of the (a) soil CO_2 fluxes (g m^{-2} d^{-1}) and (b) T (°C) from the Leirhnukur. The distribution of the data (black circles) is modeled with the overlap of 2 lognormal populations (A and B) by an EM algorithm (section 2.2.1). Both datasets are almost equally clustered in a low-CO_2 flux -and low-T-population (A, orange curve), and a high-CO_2 flux -and high-T population (B, purple curve). The light blue circles in the Q-Q plot are 100 distributions sampled from the modeled A-B mixing distribution. (For interpretation of the references to colour in this figure legend, the reader is referred to the web version of this article.)

Table 2
Carbon and oxygen isotopes of calcites recovered from drill cuttings and of the hydrothermal fluids from which precipitate in isotopic equilibrium. $\delta^{13}C_{CO2}$ and $\delta^{13}C_{H2O}$ are calculated through Eqs. (1),2 using the formation temperatures of each well at the specific depth of the cutting. Locations of the calcite samples are also reported and refer to the WGS 84/UTM zone 28 N.

well	Easting [m]	Northing [m]	elevation [m]	T [°C]	$\delta^{18}O_{CaCO3}$ [‰ SMOW]	$\delta^{18}O_{H2O}$ [‰ SMOW]	$\delta^{13}C_{CaCO3}$ [‰ PDB]	$\delta^{13}C_{CO2}$ [‰ PDB]
IDDP-1	419,042	7,289,339	432	168	−0.93	−12.31	−4.18	−4.60
IDDP-1	419,042	7,289,339	130	167	−1.57	−13.05	−4.01	−4.48
IDDP-1	419,042	7,289,339	−230	165	−5.09	−16.67	−3.93	−4.45
IDDP-1	419,042	7,289,339	−500	306	−5.85	−11.24	−5.13	−3.26
IDDP-1	419,042	7,289,339	−750	327	−3.81	−8.64	−3.55	−1.54
KJ-37	420,100	7,288,186	−106	256	−5.91	−12.96	−3.60	−2.25
KJ-37	420,070	7,288,227	−194	265	−8.49	−15.21	−3.79	−2.33
KJ-37	420,021	7,288,291	−326	277	−2.07	−8.38	−2.67	−1.07
KJ-39	419,128	7,288,194	267	202	−8.43	−17.85	−3.31	−2.88
KJ-39	419,128	7,288,194	261	204	−13.21	−22.55	−4.60	−4.13
KJ-39	419,128	7,288,194	241	208	−7.70	−16.81	−2.80	−2.23
KJ-39	419,141	7,288,196	54	240	−9.32	−16.99	−4.08	−2.95
KJ-39	419,194	7,288,178	−169	264	−5.45	−12.20	−1.67	−0.22
KJ-39	419,259	7,288,143	−315	276	−4.95	−11.28	−2.54	−0.95
KJ-39	419,430	7,288,046	−650	299	−9.11	−14.72	−4.20	−2.39
KJ-39	419,505	7,288,000	−806	308	−7.24	−12.60	−3.96	−2.08
KT-40	419,858	7,289,335	588	100	−1.01	−18.08	−0.80	−4.18
KT-40	419,858	7,289,336	540	140	−0.56	−13.95	−2.71	−4.12
KT-40	419,860	7,289,337	416	191	−2.04	−12.05	−4.42	−4.23
KT-40	419,860	7,289,336	361	202	−4.28	−13.70	−3.08	−2.64
KT-40	419,886	7,289,313	71	210	−8.09	−17.11	−3.77	−3.16
KT-40	419,938	7,289,260	−118	249	−3.03	−10.34	−3.66	−2.40
KT-40	419,969	7,289,222	−211	279	−3.67	−9.89	−3.05	−1.42
KT-40	420,042	7,289,115	−468	288	−6.76	−12.70	−5.00	−3.29

4.3. The soil CO_2 emission tracks the upflow of hydrothermal fluids with a significant thermal energy

The magmatic-hydrothermal CO_2 emission from the soils of the Suðurhlíðar subfield (green perimeter in Fig. 6) accounts for ~33.1 t d^{-1} ($\dot{m}_{CO_2}$ = 0.38 kg s^{-1}), and flows towards the surface together with 55 ± 15 kg s^{-1} of vapor separated through boiling of the hydrothermal liquid (Fig. 8; Table 3). The condensation of this vapor in the subsurface

releases a thermal energy of 144 ± 40 MW (Fig. 8; Table 3). These estimates were performed through Eqs. (3–4), by using the H$_2$O/CO$_2$ ratio in the dry steams of Suðurhlíðar borehole (KJ-14, 19, 20, 30, 31; from Hauksson, 2019, 2020, 2021; Table 3) as representative of the vapor phase before condensation. The IDDP-1 drilling suggests that the boiling zones from which CO_2-bearing vapor separated may form through the depressurization of an underlying parental fluid in a supercritical state (Scott et al., 2022). Assuming a similar fluid in the subsurface of
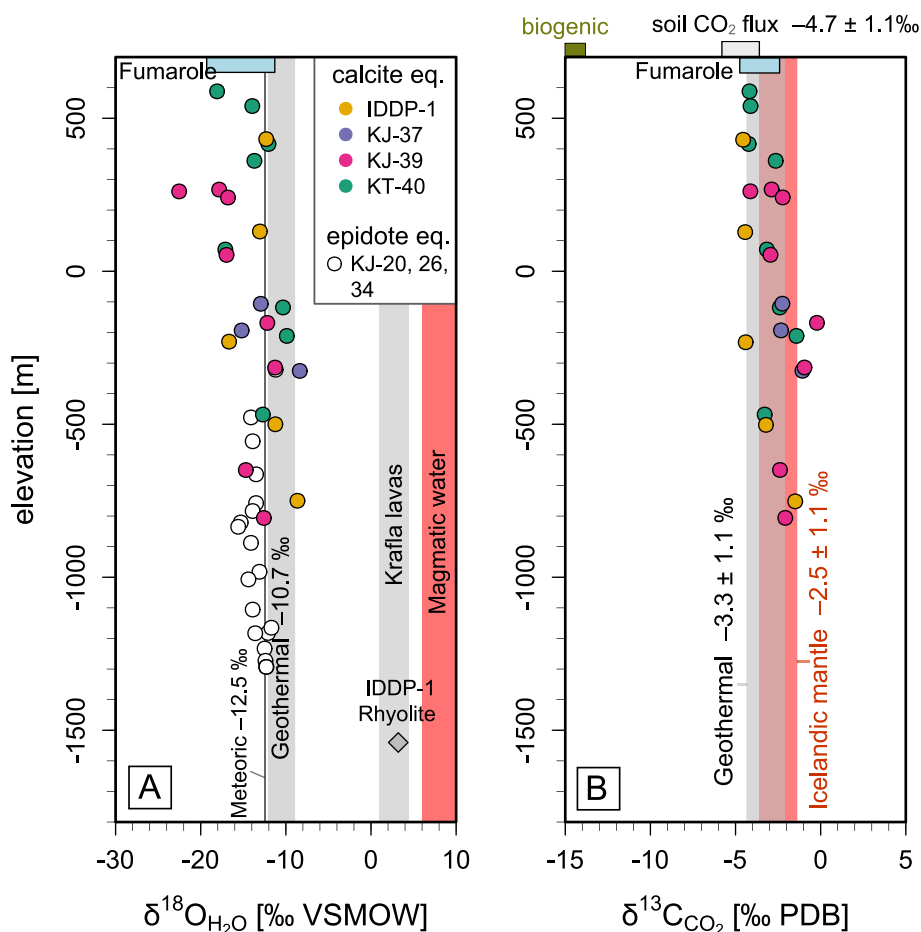
Fig. 10. Oxygen and carbon isotopes of the hydrothermal fluids from which calcite precipitated at equilibrium with depth. The isotopic compositions are calculated through Eqs. (1) and (2), using O and C isotopes of the calcite samples recovered at specific depths during the drilling of IDDP-1, KJ-37, KJ-39, and KT-40 wells, and the correspondent formation temperatures (Fig. 3). O isotopes of the fluids in equilibrium with epidotes found in KJ-20, 26, and 34 from Pope et al. (2016) are also shown for comparison. $\delta^{18}O_{H2O}$ does not show any significant trend with depth and its composition approaches that of the local meteoric water recharge (−12.5 ‰; Sveinbjörnsdóttir et al., 1986; Darling and Ármannsson, 1989). A few fluid samples show the same composition of the current geothermal liquid reservoir (−10.7 ± 0.9 ‰; average of Pope et al. (2016) and Ricci et al. (2022) data), originating from a predominant meteoric component that reacts with basaltic rocks and/or mixes with magmatic fluids. Fumarole steam condensates (Darling and Ármannsson, 1989), the IDDP-1 rhyolite glass (3.2 ± 0.2 ‰; Elders et al., 2011), unaltered Krafla lavas (both rhyolitic and basaltic, 1.0–4.5 ‰; Nicholson et al., 1991; Pope et al., 2013; Troch et al., 2020), and primary magmatic water (5–10 ‰; Giggenbach, 1992) are also shown for comparison. $\delta^{13}C_{CO2}$ is very similar to that reported from borehole fluids (−3.3 ± 1.1 ‰; average of the data of Ármannsson (1998), Barry et al. (2014), and Beaudry et al. (2021)), and approaches that of the Icelandic mantle (Barry et al., 2014) as depth increases. Mixing with local meteoric water may partly affect the composition of shallower fluids in equilibrium with calcite. The range of fumarole gases (−2.4 to −4.8 ‰; Barry et al., 2014) and both the magmatic-hydrothermal and biogenic population of soil CO_2 fluxes (Fig. 7b) are also reported.

Table 3

Mass flow and thermal energy released from steam condensation in the Suðurhlíðar subsurface. These are calculated through eqs. 3–4, using the H_2O/CO_2 weight ratio in the vapor phases discharges from the boreholes of Suðurhlíðar subfield (from Hauksson, 2019, 2020, 2021), which are practically dry steams (as shown by their enthalpy and liquid fraction f_L calculated through enthalpy and mass balances). T_S and P_S are the sampling temperature and pressure, and h is the specific enthalpy of the fluid. The mass and thermal energy flows are calculated using the soil CO_2 emission from Suðurhlíðar (green perimeter in Fig. 6), that is 33.1 t d^{-1} ($\dot{m}_{CO_2}$ = 0.38 kg s^{-1}).

well	date	T_S [°C]	P_S [bar]	h [kJ kg^{-1}]	f_L	$(C_{H2O}/C_{CO2})_V$	$\dot{m}_{H_2O,cond}$ [kg s^{-1}]	$\dot{E}_{H_2O,cond}$ [MW]
KJ-20	12.06.2018	177.6	9.5	2700	0.04	83.9	32.1	84.5
KJ-30	12.06.2018	177.6	9.5	2763	0.01	128.4	49.2	129.5
KJ-31	12.06.2018	180.9	10.2	2787	0.00	212.6	81.5	214.3
KJ-14	21.05.2019	175.4	9.0	2572	0.10	159.6	61.2	160.9
KJ-20	21.05.2019	175.8	9.1	2722	0.03	110.3	42.3	111.2
KJ-30	22.05.2019	186.8	11.7	2768	0.01	166.9	64.0	168.3
KJ-31	22.05.2019	183.5	10.9	2789	0.00	124.2	47.6	125.2
KJ-14	07.06.2021	184.0	11.0	2740	0.02	139.9	53.6	141.0
KJ-20	08.06.2021	184.6	11.1	2627	0.08	88.4	33.8	89.1
KJ-31	08.06.2021	188.6	12.2	2780	0.00	141.6	54.2	142.7
KJ-30	08.06.2021	193.9	13.4	2713	0.04	160.8	61.6	162.1
KJ-19	08.06.2021	180.1	10.0	2646	0.07	196.9	75.4	198.4
Mean						**143 ± 39**	**55 ± 15**	**144 ± 40**

Suðurhlíðar, which is supported by the occurrence of shallow rhyolitic reservoirs in both areas and recent numerical simulations (Scott et al., 2022), the molality of the fluids tapped by the IDDP-1 (from Heřmanská et al., 2019; Table 4) can be used together with the soil CO_2 emission to estimate their mass and thermal flows (Eqs. (5–6)). Notably, the ascent of 243 ± 56 kg s^{-1} of fluids with a thermal energy of 778 ± 180 MW (Fig. 8; Table 4) might feed the soil CO_2 emission from Suðurhlíðar.

5. Discussion

5.1. Magmatic-hydrothermal CO₂ emission from soils and thermal energy of the hydrothermal system

The soil CO_2 emission, T, and $\delta^{13}C_{CO2}$ measured over the Krafla geothermal field in 2022 are grouped into magmatic-hydrothermal and biologic counterparts through unsupervised clustering (*section 3.2.1*), enabling us to better constrain the spatial distribution and emission of volcanic CO_2. The biogenic production of CO_2 accounts for ~4.3 g m^{-2} d^{-1} (population A; Figs. 5b, 9a; Table 1) in both areas, consistent with that reported in the literature (~6 g m^{-2} d^{-1}, Table 1; Ármannsson et al., 2007; Dereinda and Armannsson, 2010), and dominates soils with background temperature of ~10 °C at 15 cm depth (Fig. 9b). In contrast, the average magmatic-hydrothermal CO_2 emission is ~1640 g m^{-2} d^{-1} from the main area and ~ 118 g m^{-2} d^{-1} from Leirhnjúkur (population B; Figs. 5, 9) and predominantly extends over soils characterized by intense argillic alteration, fumarolic vents, and temperatures close to the water boiling point. The main area also shows an intermediate population, likely ascribed to the mixing of the biologic and magmatic-hydrothermal CO_2 (Fig. 5b). These two C sources are clearly discriminated through the $\delta^{13}C_{CO2}$, revealing that the high-CO_2 fluxes have a magmatic-like signature of −4.7 ± 1.1 ‰ (Figs. 5b, 7), whereas low emissions point towards negative values typical of soil respiration processes. Notably, most of the magmatic-hydrothermal CO_2 fluxes discriminated through the $\delta^{13}C_{CO2}$ (Fig. 7b) overlaps with those revealed by clustering (Fig. 5), therefore attesting to the consistency of these two techniques in deciphering the magmatic-hydrothermal gas source.

The emission of magmatic-hydrothermal CO_2 from the main area accounts for about 62.5 t d^{-1} and is strongly controlled by tectonics, following the local normal faults parallel to the NNE-SSW axial direction of the rift and a WNW-ESE trend (Fig. 6a, 2). This amount of CO_2 separates through boiling of the hydrothermal liquid and is channelized towards the surface through these fractures together with a water vapor dominated phase. Approaching the surface, the steam condenses and heats the soil, while the relatively low-soluble CO_2 escapes into the atmosphere (Chiodini et al., 2005). This process is supported by the good spatial correlation between the high soil CO_2 fluxes and temperatures (Fig. 6). In particular, the highest soil T and the best correlation with the soil CO_2 flux is in the Suðurhlíðar subfield (Fig. 6), where boiling conditions are measured along the entire borehole depths, from the surface to ~2500 m, reaching 350 °C (KJ-37 and KJ-39 in Fig. 3; Mortensen et al., 2015; Scott et al., 2022). The lower soil temperatures measured in

the Vesturhlíðar subfield (Fig. 6b) suggest that the subsurface vapor condensation may occur at deeper levels. The cause appears to be the mixing with cold recharge water, which predominantly flows along a NW-SE hydrological gradient (Pope et al., 2016; Scott et al., 2022), but also downflow from the slope of Mount Krafla. This cooling is also reflected in the temperature measured downhole in the Vesturhlíðar subfield (e.g., KT-40 in Fig. 3), which sometimes shows a relatively shallow sub-boiling zone (Mortensen et al., 2015; Scott et al., 2022), similar to that observed in all Leirbotnar boreholes (e.g., IDDP-1 in Fig. 3; *section 2*). The heat subtracted from the system by the heated meteoric water outflow may therefore be substantial in the northern part of the main area (Fig. 6), and should be taken into account for modeling the total thermal budget of the geothermal system. In addition, we cannot exclude that part of the ascending CO_2 is removed and transported by the meteoric water outflow in Vesturhlíðar, whereas this process should be negligible in Suðurhlíðar, as suggested by the hot soils from which CO_2 escapes.

We therefore focused the mass and thermal flow computation (*section 3.4*) in the Suðurhlíðar subfield (green perimeter in Fig. 6), where soil CO_2 flux and T are best correlated (Fig. 8) and dissolution of CO_2 in shallow aquifers appears negligible. Considering a soil CO_2 emission of ~0.38 kg s^{-1} (33 t d^{-1}), the mass flow of the condensed steam in the Suðurhlíðar subsurface and the correspondent energy release is estimated at 55 ± 15 kg s^{-1} and 144 ± 40 MW (Table 3; Fig. 8). This amount of energy (224 W m^{-2}) is higher than the average thermal release estimated with the same technique in other worldwide volcanoes (131 W m^{-2}; Campi Flegrei, Ischia, Vesuvio, Vulcano, Pantelleria, Masaya, Yellowstone, Nisyros, Copahue, Furnas do Enxofre, and Peteroa; Chiodini et al., 2021). Interestingly, the heat released from Reykjanes soils through subsurface steam condensation is higher (578 W m^{-2}; Fridriksson et al., 2006) than that estimated from Suðurhlíðar. Above the shallow magmatic intrusions encountered at Krafla, the vapor and CO_2 separate from boiling zones that are thought to form through the ascent and decompression of underlying supercritical fluids (Fig. 8; Scott et al., 2022). According to our estimates, the Suðurhlíðar subsurface might host an upflow and depressurization of 243 ± 56 kg s^{-1} of fluids with a thermal energy of 778 ± 180 MW (Table 4; Fig. 8). This amount of energy is far high than that of the upflowing hydrothermal liquid feeding the soil CO_2 emission in conventional hydrothermal systems. For example, the soil degassing process at the Nisyros caldera (South Aegean Volcanic Arc, Greece) is sustained by the ascent of liquids at 340 °C with a thermal energy of 130–270 MW (Bini et al., 2019). Such significant amount of energy may be located not only below Suðurhlíðar but also in Vitismór (IDDP-1 location; Fig. 1), where shallow magma reservoirs were encountered and supercritical fluids are thought to form through isobaric heating of meteoric water (Heřmanská et al., 2019; Scott et al., 2022; Fig. 8). However, it is still not clear if these are isolated melt pockets or if a continuous shallow reservoir exists at shallow depth below the geothermal field. If supercritical conditions extended in the subsurface of all the main area investigated through soil CO_2 flux measurements, the thermal energy could be on the order of 1.5 GW (Table 4).

Table 4

Mass flow and thermal energy of fluids feeding the diffuse degassing of CO_2 from Krafla soils. The molality of CO_2, H_2O flow, and thermal energy are calculated through Eqs. (5–6), using the chemical composition of supercritical fluids from Heřmanská et al. (2019). T_S and P_S are the sampling temperature and pressure, and h is the specific enthalpy of the fluid. The mass and thermal energy flows are calculated using a soil CO_2 emission of 33.1 t d^{-1} ($\dot{n}_{CO_2}$ = 8.7 mol s^{-1}) for Suðurhlíðar, and 62.5 t d^{-1} ($\dot{n}_{CO_2}$ = 16.4 mol s^{-1}) for the main production area.

Sample	well	T_S [°C]	P_S [bar]	h [kJ kg^{-1}]	m_{CO_2} [mol kg^{-1}]	Suðurhlíðar $\dot{m}_{H_2O}$ [kg s^{-1}]	Suðurhlíðar $\dot{E}_{H_2O}$ [MW]	Main area $\dot{m}_{H_2O}$ [kg s^{-1}]	Main area $\dot{E}_{H_2O}$ [MW]
12-KRA-01	IDDP-1	440	140	3200	0.0479	182	582	343	1098
12-KRA-02	IDDP-1	440	140	3200	0.0298	292	935	552	1765
12-KRA-03	IDDP-1	440	140	3200	0.0341	255	817	482	1542
Mean					**0.0373 ± 0.0095**	**243 ± 56**	**778 ± 180**	**459 ± 106**	**1469 ± 340**

5.2. $\delta^{13}C$ of CO_2 and $CaCO_3$ reflects the magmatic source of the Icelandic mantle

Magmatic-hydrothermal systems are characterized by complex processes that may alter the original elemental and isotopic composition of CO_2 (Stefánsson et al., 2016), such as phase separation, calcite precipitation, and mixing with surface water. Therefore, the C isotopes of deep calcite samples recovered from boreholes at different depths may help us to better understand the $\delta^{13}C$ signature of the soil CO_2 emission. Among the processes mentioned above, C isotopes positively fractionate (~2 ‰) during volatile exsolution from basaltic magmas at 1200–1400 °C, producing a more positive $\delta^{13}C$ in the exsolved gas phase (Mattey, 1991). At lower temperatures (>192 °C), akin to the hydrothermal environment, calcite precipitation also increases the $\delta^{13}C$ of the CO_2 dissolved in the fluid, whereas below 192 °C the fractionation is reversed (Bottinga, 1968, 1969). The deepest calcite samples reveal that the fluid in equilibrium had $\delta^{13}C_{CO_2}$ values very similar to that of the Icelandic mantle (−2.5 ± 1.1 ‰; Barry et al., 2014; Fig. 10b; Table 2), suggesting less negative values as depth increases. Interestingly, these samples were recovered from the two geothermal wells that encountered shallow rhyolitic melts (~2 km depth) during drilling operations, that is KJ-39 and IDDP-1. This magmatic fluid composition is still predominant at shallower depths but appears to slightly decrease as the fluids approach the surface (Fig. 10b). These more negative $\delta^{13}C_{CO_2}$ values might be due to mixing with local groundwater, whose light carbon signature mainly derives from biological and atmospheric sources. However, the mean $\delta^{13}C_{CO_2}$ of all the calcites from different depths (−2.8 ± 1.2 ‰) still overlaps the Icelandic mantle and the $\delta^{13}C_{CO_2}$ of the geothermal fluid composition of Krafla (−3.3 ± 1.1 ‰; Ármannsson, 1998; Barry et al., 2014; Beaudry et al., 2021; Fig. 10b). More generally, it also overlaps the average geothermal fluid composition of the Icelandic neovolcanic zone (−3.1 ± 1.9 ‰; Barry et al., 2014).

A few soil CO_2 fluxes from the Suðurhlíðar subfield (*n* = 8) show the same $\delta^{13}C$ signature of the Icelandic magmatic fluids recorded in the deep calcite samples (Fig. 6a). The remaining magmatic-hydrothermal CO_2 fluxes are clustered in a population with $\delta^{13}C$ values slightly lighter (−4.7 ± 1.1 ‰; Fig. 7b) than that of the magmatic endmember (Fig. 10b). This may be the effect of the cold recharge water, more pronounced in the Vesturhlíðar subfield with respect to the Suðurhlíðar area (see *section 5.1*). Since the clustered population also shows $\delta^{13}C_{CO_2}$ slightly lighter than those of the geothermal fluids (fumarole and borehole; Fig. 10b), we cannot exclude some influence of shallower biogenic gas from soil respiration or transported by the groundwater. Despite slight modification due to these processes, the $\delta^{13}C$ signature of the clustered population (−4.7 ± 1.1 ‰; Fig. 7b) shows a clear predominant contribution from the Icelandic mantle (Fig. 10b).

Oxygen isotopes show that the predominant source of the fluids in equilibrium with calcite samples is the local meteoric water recharge, with a limited contribution from magmatic water (Fig. 10a). Similar to the $\delta^{13}C_{CO_2}$, the contribution of magmatic fluids appears to slightly increase with depth (Fig. 10a). In this context, it is worth noting that the deepest sample of IDDP-1, which was drilled into a shallow pocket of rhyolitic melt, shows the greatest magmatic contribution (together with a shallower sample of KJ-37; Fig. 10a), as also registered by its $\delta^{13}C_{CO_2}$ (Fig. 10b). A few calcite samples appear to precipitate at equilibrium with the geothermal liquid (Fig. 10a), whose $\delta^{18}O_{H2O}$ is slightly positive with respect to the meteoric water due to fluid-rock interactions or magmatic fluid addition. However, the geothermal liquid fails in explaining most of the samples recovered at shallow depths, showing more negative $\delta^{18}O_{H2O}$ (Fig. 10a). These lighter values may reflect steam separation through boiling of deeper liquids, upflow, condensation, and mixing with shallower liquids, before calcite precipitation. This process was previously suggested by Pope et al. (2016) for explaining the light $\delta^{18}O_{H2O}$ of the fluids in equilibrium with epidote samples recovered from drill cuttings (white circles in Fig. 10a). Due to the extensive C isotope fractionation at low temperatures, this process may have

stronger effects at shallow depths. The potential light signature of such steam, generated by the O isotope exchange between the liquid and the vapor phase during boiling, is also supported by the fumarole steam condensate data (Darling and Ármannsson, 1989; Fig. 10a).

5.3. Increase in the CO_2 emission from 2004-2008 to 2022

The soil CO_2 emission from the main area (62.5 t d^{-1}) is significantly higher than that measured in 2004–2008 (~22 t d^{-1}; Ármannsson et al., 2007), while the geometry of the degassing structures has remained almost the same (Fig. 6a; see Fig. 2 in Ármannsson et al., 2007). In particular, the two WNW-ESE structures in the Suðurhlíðar area and the NNE-SSW structure in the Vesturhlíðar subfield appear to degas significantly higher amounts of CO_2. This is suggested by their greater extent (Fig. 6a) and the value of the hydrothermal population in 2022 (1641 ± 614 g m^2 d^{-1}; Fig. 5; Table 1), which is one order of magnitude higher than that of 2004–2008 (~115 g m^2 d^{-1}; Ármannsson et al., 2007; Table 1). A few soil CO_2 fluxes measured along transects in 2014 and 2017 (Kristinsson et al., 2014, 2017) overlap the hydrothermal population of 2022, suggesting that the soil CO_2 increase might have occurred before. However, the spatial uncertainty associated with the monitoring of single-point alignments over different years, and the absence of soil CO_2 flux measurements over an areal extent and their statistical elaborations (soil CO_2 flux map, estimate of the CO_2 output, and clustered populations of soil CO_2 fluxes) in 2014–2017, prevent us from unambiguously comparing these data with those of 2004–2008 and 2022. Hence, we focus the comparison between 2004– 2008 and 2022 periods. Since both areas were investigated with the same techniques over comparable spatial extents during the two campaigns, these variations cannot be ascribed to methodological bias or geometry conditions but appear to be related to other processes.

The increase in the CO_2 emitted into the atmosphere from Krafla soils between 2004– 2008 and 2022 suggests changes either in the magmatic dynamics or in the geothermal fluid utilization. These two causes were also suggested by Hersir et al. (2020) to explain a recent inflation-deflation sequence and changes in the seismic activity occurred between 2018 and 2020. In this period, a vertical ground uplift was measured between Leirhnjúkur and the IDDP-1 well, together with a southward displacement, while seismic activity becomes less frequent but with larger events (Hersir et al., 2020). The CO_2 concentration of the geothermal fluids (fumarole and borehole fluids) from the main production area shows an almost constant value between the two soil CO_2 campaigns (Óskarsson et al., 2019). Since CO_2 concentrations registered a remarkable increase during the last eruptive activity of the Krafla Fires (Ármannsson et al., 1989) — the CO_2 concentration of the well KJ-7 increased up to ~5.5% in 1976–1978, during a main eruptive phase of the Krafla Fires, and then slowly decreased down to pre-eruptive values of ~0.2% in 1984 — this almost stationary trend does not suggest new magmatic activity. However, it is worth noting that chemical changes due to new intrusions or episodes of magmatic outgassing may need several months before being revealed at the surface (e.g., Ármansson 1989, Chiodini et al., 2015b, Bini et al., 2022), depending on the thickness of the hydrothermal aquifer.

Interestingly, both the total mass of fluid extracted from the geothermal system and the CO_2 emission into the atmosphere from the power plant has decreased in 2021 (213 kg s^{-1} and 68 t d^{-1}) with respect to 2004–2008 (277–361 kg s^{-1} and 130–122 t d^{-1}; Baldvinsson et al., 2011; Hauksson, 2021; Arnarson, 2022). Part of this drop focuses on the 2018–2020 period, when production from low-enthalpy water-rich fluids was reduced for optimization reasons, the net amount of fluid extracted from the Leirbotnar subfield (production minus reinjection) decreased, and the pressure and water level in a monitoring well at 800 m depth (KG-10) showed an increase of 2 bar and 25 m (Egilson, 2020; Hersir et al., 2020). Reinjection was also variable in time and space during this period (from wells KJ-26, 35, and 39), but generally slightly decreased over time, while no correlation between changes in

reinjection and seismic activity was found (Blanck et al., 2020). A general decrease in the mass extracted from the main production area of the geothermal system may imply a reduction in the CO_2 emission from the power plant and induce a pressure buildup in the reservoir, and consequently larger natural emission of CO_2 from soils into the atmosphere. In particular, since the impermeable aquitard in the Leirbotnar subsurface tends to channelize the geothermal fluids through both the Hvergil fissure and the Suðurhlíðar subfield (Fig. 2; Ármannsson et al., 1989; Pope et al., 2016; Scott et al., 2022), it is possible that the decrease in the fluid extracted from Leirbotnar increased the soil CO_2 emissions from these areas.

Local effects might have also contributed to the increase in the soil CO_2 emission, but unfortunately the scarcity of published data make us unable to draw conclusions on their control on such variation. For example, the stop of reinjection through KJ-39 in summer 2021 was followed by an increase in both steam flows and boiling from the Suðurhlíðar subfield (Personal communication from Landsvirkjun, May 2023), which might correlate with higher soil CO_2 fluxes, and implying a subsurface heating. The increase in the CO_2 emission from Vesturhlíðar might instead be related to fluid utilization from this area (from the eruptive fissure targeted by well KT-40; Fig. 6a) started in 2009, that is one year after the last soil CO_2 flux survey. This control of the geothermal utilization on soil degassing is well documented in the Reykjanes geothermal field (Iceland). Yearly measurements of the soil CO_2 flux over a target area of 220,000 m^2 show that the diffuse emission gradually increased from 13.5 t d^{-1} in 2004 to 51.4 t d^{-1} in 2013, and inversely correlates with the CO_2 emitted due to power generation (Óladóttir and Friðriksson, 2015; Fridriksson et al., 2017). Among the possible causes, these authors suggested a pressure drawdown in the system after a 100 MWe power plant was commissioned in 2006. In conclusion, all these indications may suggest a possible increase in the natural soil CO_2 emission from the main production area of Krafla due to the variation in the production strategy. However, given the low frequency of the soil CO_2 monitoring at Krafla, it is difficult to precisely discern a magmatic-hydrothermal or anthropogenic-induced cause. A more detailed comparison of the soil CO_2 emission with the geochemistry of the fluids, geophysical information, and geothermal utilization data is needed to better understand this variation.

6. Conclusions

The soil CO_2 emission and temperature measured at Krafla in 2022 shows that the hydrothermal fluid upflow is focused through the tectonic structures of the neovolcanic rift zone (Fig. 6a). This is in good agreement with previous knowledge about the hydrothermal fluid circulation at Krafla and its hydrology (e.g., Fig. 2). In particular, while the shallower part of the Vesturhlíðar subsurface appear to be cooled down by the meteoric water recharge flow, the Suðurhlíðar subfield is less affected by this process and shows boiling conditions everywhere in the subsurface. This is highlighted by the spatial correlation between soil T and CO_2 flux in Suðurhlíðar, which in contrast is less evident in Vesturhlíðar (Fig. 6).

Calcite samples recovered at 1400 m depth below Suðurhlíðar record a clear $\delta^{13}C$ magmatic signature of the Icelandic mantle (Fig. 10b), which likely outgassed from the shallow magma reservoir tapped a few hundred meters below during the drilling of KJ-39. The upflow of magmatic fluids through this subfield is also revealed at the surface by the $\delta^{13}C$ of the soil CO_2 emission (Fig. 6a). Given the evidence of supercritical conditions forming in the surroundings of shallow magma reservoirs at Krafla (e.g., IDDP-1), the soil CO_2 degassing of Suðurhlíðar might also be fed by supercritical fluids with a thermal energy estimated at ~800 MW (Fig. 8). Despite the strong magmatic C signature of the fluids circulating in this subfield, $\delta^{13}C$ of the CO_2 emission and calcites reveal a predominant magmatic origin in the whole area investigated. Hence, the hydrothermal fluid flow in Leirbotnar, Vesturhlíðar, Suðurhlíðar, and Leirhnjúkur might be driven by a common magmatic

source. If the two melt pockets intercepted by IDDP-1 and KJ-39 wells reflected just a portion of a magma reservoir below the central part of the caldera, supercritical fluids may be more extensive than previously thought, and the thermal energy associated with their upflow could be remarkable (~1.5 GW below the main production area).

Finally, we noted a significant increase in the soil CO_2 fluxes in 2022 with respect to 2004–2008 (62.5 vs. 22 t d^{-1}). This could be ascribed to variation in the geothermal production rather than new magmatic activity, and might have started concurrently with recent ground deformations (2018–2020), or even before. New data and a more detailed comparison with geophysical, geochemical, and productivity information are needed to better distinguish the cause. The soil CO_2 emission and the $\delta^{13}C$ of both efflux and hydrothermal calcite have therefore important implications for both magmatic-hydrothermal monitoring and geothermal exploration, as can help us to quantify and track the upflow zones of magmatic gases and the associated high-enthalpy fluids.

CRediT authorship contribution statement

Giulio Bini: Conceptualization, Data curation, Formal analysis, Investigation, Visualization, Writing – original draft, Writing – review & editing. **Giovanni Chiodini:** Conceptualization, Formal analysis, Writing – review & editing. **Tullio Ricci:** Investigation, Writing – review & editing. **Alessandra Sciarra:** Investigation, Resources, Writing – review & editing. **Stefano Caliro:** Investigation, Resources, Writing – review & editing. **Anette K. Mortensen:** Resources, Writing - review & editing. **Marco Martini:** Investigation, Resources. **Andrew Mitchell:** Investigation. **Alessandro Santi:** Investigation. **Antonio Costa:** Funding acquisition, Writing – review & editing.

Declaration of competing interest

The authors declare that they have no known competing financial interests or personal relationships that could have appeared to influence the work reported in this paper.

Data availability

Data are available as supplementary material.

Acknowledgements

Appendix A. Supplementary data

Supplementary data to this article can be found online at https://doi.org/10.1016/j.jvolgeores.2024.108032.

References

Ármannsson, H., 1998. Öxarfjördur. Studies of Gas. Orkustofnun OS-98051, p. 14.
Ármannsson, H., Benjamínsson, J., Jeffrey, A.W.A., 1989. Gas changes in the Krafla geothermal system, Iceland. Chem. Geol. 76, 175–196.

Ármannsson, H., Fridriksson, T., Wiese, F., Hernández, P., Pérez, N., 2007. CO_2 budget of the Krafla geothermal system, NE-Iceland. In: Bullen, T.B., Wang, Y. (Eds.), Water-Rock Interaction. Taylor & Francis Group, London, pp. 189–192.

Arnarson, 2022. Climate Account 2021, Landsvirkjun. Retrieved on May 2023 from: https://www.landsvirkjun.com/api/get-pdf?id=2a2a7c87-9233-4a14-a928-a3d75 67ae5cf_LV_Climate_Accounts_2021_V12.pdf&name=LV_Climate_Accounts_2021_V 12.pdf.

Árnason, K., 2020. New Conceptual Model for the Magma-Hydrothermal-Tectonic System of Krafla, NE Iceland. Geosciences 10, 34.

Baldvinsson, I., Thórisdóttir, T.H., Ketilsson, J., 2011. Gas Emissions from Geothermal Power Plants in Iceland 1970 to 2009. National Energy Authority. OS-2011/02 (in Icelandic).

Barry, P.H., Hilton, D.R., Füri, E., Halldórsson, S.A., Grönvold, K., 2014. Carbon isotope and abundance systematics of Icelandic geothermal gases, fluids and subglacial basalts with implications for mantle plume-related CO_2 fluxes. Geochim. Cosmochim. Acta 134, 74–99.

Beaudry, P., Stefánsson, A., Fiebig, J., Rhim, J.H., Ono, S., 2021. High temperature generation and equilibration of methane in terrestrial geothermal systems: Evidence from clumped isotopologues. Geochim. Cosmochim. Acta 309, 209–234.

Benaglia, T., Chauveau, D., Hunter, D.R., 2009. An EM-Like Algorithm for Semi- and Nonparametric Estimation in Multivariate Mixtures. J. Comput. Graph. Stat. 18, 505–526.

Bini, G., Chiodini, G., Cardellini, C., Vougioukalakis, G.E., Bachmann, O., 2019. Diffuse emission of CO_2 and convective heat release at Nisyros caldera (Greece). J. Volcanol. Geotherm. Res. 376, 44–53.

Bini, G., Chiodini, G., Lucchetti, C., Moschini, P., Caliro, S., Mollo, S., Selva, J., Tuccimei, P., Galli, G., Bachmann, O., 2020. Deep versus shallow sources of CO_2 and Rn from a multi-parametric approach: the case of the Nisyros caldera (Aegean Arc, Greece). Sci. Rep. 10, 13782.

Bini, G., Chiodini, G., Caliro, S., Tassi, F., Vaselli, O., Rizzo, A.L., Mollo, S., Vougioukalakis, G.E., Bachmann, O., 2022. Nitrogen, helium, and argon reveal the magmatic signature of fumarole gases and episodes of outgassing from upper-crustal magma reservoirs: The case of the Nisyros caldera (Aegean Arc, Greece). Geochim. Cosmochim. Acta 335, 68–84.

Blanck, H., Ágústsdóttir, F., Ágústsson, K., Gunnarsson, K., 2020. Seismic Monitoring in Krafla, Námafjall and fleistareykir. Iceland GeoSurv. ÍSOR-2020/003, LV-2020-003.

Bottinga, Y., 1968. Calculation of fractionation factors for carbon and oxygen isotopic exchange in the system calcite-carbon dioxide-water. J. Phys. Chem. 72, 800–808.

Bottinga, Y., 1969. Calculated fractionation factors for carbon and hydrogen isotope exchange in the system calcite-carbon dioxide-graphite-methane-hydrogen-water vapor. Geochim. Cosmochim. Acta 33, 49–64.

Cardellini, C., Chiodini, G., Frondini, F., 2003. Application of stochastic simulation to CO_2 flux from soil: Mapping and quantification of gas release. J. Geophys. Res. 108.

Cardellini, C., Chiodini, G., Frondini, F., Avino, R., Bagnato, E., Caliro, S., Lelli, M., Rosiello, A., 2017. Monitoring diffuse volcanic degassing during volcanic unrests: the case of Campi Flegrei (Italy). Sci. Rep. 7, 6757.

Cheng, W., 1996. Measurement of rhizosphere respiration and organic matter decomposition using natural 13C. Plant Soil 183, 263–268.

Chiodini, G., Cioni, R., Guidi, M., Raco, B., Marini, L., 1998. Soil CO_2 flux measurements in volcanic and geothermal areas. Appl. Geochem. 13, 543–552.

Chiodini, G., Granieri, D., Avino, R., Caliro, S., Costa, A., Werner, C., 2005. Carbon dioxide diffuse degassing and estimation of heat release from volcanic and hydrothermal systems. J. Geophys. Res. 110, B08204.

Chiodini, G., Baldini, A., Barberi, F., Carapezza, M.L., Cardellini, C., Frondini, F., Granieri, D., Ranaldi, M., 2007. Carbon dioxide degassing at Latera caldera (Italy): evidence of geothermal reservoir and evaluation of its potential energy. J. Geophys. Res. Solid Earth 112 (B12).

Chiodini, G., Caliro, S., Cardellini, C., Avino, R., Granieri, D., Schmidt, A., 2008. Carbon isotopic composition of soil CO_2 efflux, a powerful method to discriminate different sources feeding soil CO_2 degassing in volcanic-hydrothermal areas. Earth Planet. Sci. Lett. 274, 372–379.

Chiodini, G., Pappalardo, L., Aiuppa, A., Caliro, S., 2015a. The geological CO_2 degassing history of a long-lived caldera. Geology 43, 767–770.

Chiodini, G., Vandemeulebrouck, J., Caliro, S., D'Auria, L., De Martino, P., Mangiacapra, A., Petrillo, Z., 2015b. Evidence of thermal-driven processes triggering the 2005–2014 unrest at Campi Flegrei caldera. Earth Planet. Sci. Lett. 414, 58–67.

Chiodini, G., Cardellini, C., Bini, G., Frondini, F., Caliro, S., Ricci, L., Lucidi, B., 2021. The Carbon Dioxide Emission as Indicator of the Geothermal Heat Flow: Review of Local and Regional Applications with a Special Focus on Italy. Energies 14, 6590.

Darling, W.G., Ármannsson, H., 1989. Stable isotopic aspects of fluid flow in the Krafla, Námafjall and Theistareykir geothermal systems of northeast Iceland. Chem. Geol. 76, 197–213.

Dereinda, F.H., Armannsson, H., 2010. CO_2 emissions from the Krafla geothermal area, Iceland. In: Proceedings World Geothermal Congress, pp. 25–29.

Deutsch, C.V., Journel, A.G., 1998. GSLIB: Geostatistical Software Library and Users Guide. Oxford Univerity Press, New York, p. 369.

Driesner, T., 2021. Supercritical and superhot geothermal resources-some fundamental insights. In: Proceedings World Geothermal Congress 2020+1.

Driesner, T., Heinrich, C.A., 2007. The system H_2O–NaCl. Part I: Correlation formulae for phase relations in temperature–pressure–composition space from 0 to 1000 °C, 0 to 5000 bar, and 0 to 1 X_{NaCl}. Geochim. Cosmochim. Acta 71 (20), 4880–4901.

Egilson, F., 2020. Eftirlitsmælingar í Kröflu, Bjarnarflagi og á fleistareykjum árið 2020. Iceland GeoSurv. report, ÍSOR-2020/038 / LV-2020-037 (In Icelandic).

Einarsson, P., 1991. Earthquakes and present-day tectonism in Iceland. Tectonophysics 189, 261–279.

Einarsson, P., 2008. Plate boundaries, rifts and transforms in Iceland. J.kull J. 58, 35–58.

Elders, W.A., Friðleifsson, G.Ó., Zierenberg, R.A., Pope, E.C., Mortensen, A.K., Guðmundsson, Á., Lowenstern, J.B., Marks, N.E., Owens, L., Bird, D.K., Reed, M., Olsen, N.J., Schiffman, P., 2011. Origin of a rhyolite that intruded a geothermal well while drilling at the Krafla volcano, Iceland. Geology 39, 231–234.

Fridriksson, T., Kristjánsson, B.R., Ármannsson, H., Margrétardóttir, E., Ólafsdóttir, S., Chiodini, G., 2006. CO_2 emissions and heat flow through soil, fumaroles, and steam heated mud pools at the Reykjanes geothermal area, SW Iceland. Appl. Geochem. 21, 1551–1569.

Fridriksson, T., Merino, A.M., Orucu, A.Y., Audinet, P., 2017. Greenhouse gas emissions from geothermal power production. In: In Proceedings, 42nd Workshop on Geothermal Reservoir Engineering. Stanford University, Stanford, California.

Friedman, I., O'Neil, J.R., 1977. Compilation of stable isotope fractionation factors of geochemical interest. In: US Geological Survey Professional Paper, 440.

Giggenbach, W.F., 1992. Isotopic shifts in waters from geothermal and volcanic systems along convergent plate boundaries and their origin. Earth Planet. Sci. Lett. 113, 495–510.

Giggenbach, W.F., 1996. Chemical Composition of Volcanic Gases. In: Monitoring and Mitigation of Volcano Hazards. Springer, Berlin Heidelberg, Berlin, Heidelberg, pp. 221–256.

Gudmundsson, Á., Mortensen, A.K., 2015. Well locations consideration of purpose, objectives and achievement with emphasis on recent drilling in the Krafla geothermal area. In: Proceedings of the World Geothermal Congress.

Hauksson, T., 2019. Þeistareykir, Krafla og Bjarnarflag, Afköst borhola og efnainnihald vatns og gufu í borholum og vinnslurás árið 2018. Report LV-2019-026. Kemía/ Landsvirkjun (In Icelandic).

Hauksson, T., 2020. Þeistareykir, Krafla og Bjarnarflag, Afköst borhola og efnainnihald vatns og gufu í borholum og vinnslurás árið 2019. Report LV-2020-010. Kemía/ Landsvirkjun (In Icelandic).

Hauksson, T., 2021. Þeistareykir, Krafla og Bjarnarflag, Afköst borhola og efnainnihald vatns og gufu í borholum og vinnslurás árið 2021. Report LV-2021-051. Kemía/ Landsvirkjun (In Icelandic).

Hayba, D.O., Ingebritsen, S.E., 1997. Multiphase groundwater flow near cooling plutons. J. Geophys. Res. 102, 12235–12252.

Heřmanská, M., Stefánsson, A., Scott, S., 2019. Supercritical fluids around magmatic intrusions: IDDP-1 at Krafla, Iceland. Geothermics 78, 101–110.

Hersir, G.P., Sigmundsson, F., Ágústsson, K., Magnússon, I.T., Drouin, V., Vilhjálmsson, A.M., Lanzi, C., Li, S., Geirsson, H., Hreinsdóttir, S., 2020. Geodetic Observations and Surface Deformation at Krafla mid 2018–2020. In: Status Report December 2020. Report ÍSOR-2020/037, RH-9-20, LV-2020-036.

Hjartardóttir, Á.R., Einarsson, P., Magnúsdóttir, S., Björnsdóttir, T., Brandsdóttir, B., 2016. Fracture systems of the northern volcanic rift zone, Iceland: An onshore part of the mid-Atlantic plate boundary. Geol. Soc. Lond., Spec. Publ. 420 (1), 297–314.

Ingason, K., Kristjánsson, V., Einarsson, K., 2014. Design and development of the discharge system of IDDP-1. Geothermics 49, 58–65.

Kristinsson, S.G., Óskarsson, F., Ólafsson, M., Óladóttir, A.A., 2014. The high Temperature Geothermal Areas in Krafla, Námafjall and Þeistareykir. Monitoring of Surface Activity and Groundwater in 2014 (In Icelandic). Iceland GeoSurvey ÍSOR-2014/058, Landsvirkjun, LV-2014-32, p. 173.

Kristinsson, S.G., Óskarsson, F., Óladóttir, A.A., Ólafsson, M., 2017. The high temperature geothermal areas in Krafla, Námafjall and Þeistareykir. Monitoring of surface activity and groundwater in 2017 (In Icelandic). In: Iceland GeoSurvey ÍSOR-2017/086, Landsvirkjun, LV-2017-123, p. 178.

Marty, B., Zimmermann, L., 1999. Volatiles (He, C, N, Ar) in mid-ocean ridge basalts: assesment of shallow-level fractionation and characterization of source composition. Geochim. Cosmochim. Acta 63, 3619–3633.

Mattey, D.P., 1991. Carbon dioxide solubility and carbon isotope fractionation in basalt melt. Geochim. Cosmochim. Acta 55, 3467–3473.

Montanaro, C., Mortensen, A.K., Weisenberger, T.B., Dingwell, D.B., Scheu, B., 2021. Stratigraphic reconstruction of the Víti breccia at Krafla volcano (Iceland): insights into pre-eruptive conditions priming explosive eruptions in geothermal areas. Bull. Volcanol. 83, 81.

Mortensen, A.K., Grönvold, K., Gudmundsson, Á., Steingrímsson, B., Egilson, F., 2010. Quenched silicic glass from well KJ-39 in Krafla, North-Eastern Iceland.

Mortensen, A.K., Gudmundsson, Á., Steingrímsson, B., Sigmundsson, F., Axelsson, G., Ármannsson, H., Hauksson, T., 2015. The Krafla geothermal system: Research summary and conceptual model revision (Tech. Rep. No. LV-2015-098). Landsvirkjun.

Nicholson, H., Condomines, M., Fitton, J.G., Fallick, A.E., Gr Nvold, K., Rogers, G., 1991. Geochemical and Isotopic Evidence for Crustal Assimilation Beneath Krafla, Iceland. J. Petrol. 32, 1005–1020.

Óladóttir, A.A., Friðriksson, Þ., 2015. The evolution of CO_2 emissions and heat flow through soil since 2004 in the Utilized Reykjanes Geothermal Area, SW Iceland: ten years of observations on changes in geothermal surface activity. In: Proceedings World Geothermal Congress.

Óskarsson, F., Ólafsson, M., Kristinsson, S.G., 2019. Háhitasvæðin á fleistareykjum, í Kröflu og Námafjalli. Vöktun á yfirborðsvirkni og grunnvatni árið 2019. In: Iceland GeoSurvey, ÍSOR-2019/077, LV-2019-081. ÍSOR/Landsvirkjun, p. 104 (In Icelandic).

Pebesma, E.J., 2004. Multivariable geostatistics in S: the gstat package. Comput. Geosci. 30, 683–691.

Pope, E.C., Bird, D.K., Arnórsson, S., 2013. Evolution of low-18O Icelandic crust. Earth Planet. Sci. Lett. 374, 47–59.

Pope, E.C., Bird, D.K., Arnórsson, S., Giroud, N., 2016. Hydrogeology of the Krafla geothermal system, northeast Iceland. Geofluids 16, 175–197.

Poreda, R.J., Craig, H., Arnorsson, S., Welhan, J.A., 1992. Helium isotopes in Icelandic geothermal systems: I. 3He, gas chemistry, and 13C relations. Geochimica et Cosmochimica Acta 56 (12), 4221–4228.

R Core Team, 2023. R: A language and environment for statistical computing. R Foundation for Statistical Computing, Vienna, Austria https://www.R-project.org/.

Ranta, E., Halldórsson, S.A., Barry, P.H., Ono, S., Robin, J.G., Kleine, B.I., Ricci, A., Fiebig, J., Sveinbjörnsdóttir, Á.E., Stefánsson, A., 2023. Deep magma degassing and volatile fluxes through volcanic hydrothermal systems: Insights from the Askja and Kverkfjöll volcanoes, Iceland. Journal of Volcanology and Geothermal Research 436, 107776.

Ricci, A., Kleine, B.I., Fiebig, J., Gunnarsson-Robin, J., Mativo Kamunya, K., Mountain, B., Stefánsson, A., 2022. Equilibrium and kinetic controls on molecular hydrogen abundance and hydrogen isotope fractionation in hydrothermal fluids. Earth Planet. Sci. Lett. 579, 117338.

Rooyakkers, S.M., Stix, J., Berlo, K., Petrelli, M., Hampton, R.L., Barker, S.J., Morgavi, D., 2021. The Origin of Rhyolitic Magmas at Krafla Central Volcano (Iceland). J. Petrol. 62 egab064.

Sæmundsson, K., 1991. Geology of the Krafla System. The Natural History of Lake Myvatn, pp. 24–95.

Sæmundsson, K., 2008. Krafla Geological Map. 1:25.000. Landsvirkjun and ÍSOR.

Sano, Y., Urabe, A., Wakita, H., Chiba, H., Sakai, H., 1985. Chemical and isotopic compositions of gases in geothermal fluids in Iceland. Geochemical journal 19 (3), 135–148.

Scott, S.W., O'Sullivan, J.P., Maclaren, O.J., Nicholson, R., Covell, C., Newson, J., Guðjónsdóttir, M.S., 2022. Bayesian Calibration of a Natural State Geothermal Reservoir Model, Krafla, North Iceland. Water Resources Research, p. 58.

Simmons, S.F., Christenson, B.W., 1994. Origins of calcite in a boiling geothermal system. Am. J. Sci. 294, 361–400.

Sinclair, A.J., 1974. Selection of threshold values in geochemical data using probability graphs. J. Geochem. Explor. 3, 129–149.

Sinclair, A.J., 1991. A fundamental approach to threshold estimation in exploration geochemistry: probability plots revisited. J. Geochem. Explor. 41, 1–22.

Stefánsson, V., 1981. The Krafla geothermal field, northeast Iceland. In: Rybach, L., Muffler, L.J.P. (Eds.), Geothermal systems: Principles and case studies. Wiley-Interscience, pp. 273–293.

Stefánsson, A., Sveinbjörnsdóttir, Á.E., Heinemeier, J., Arnórsson, S., Kjartansdóttir, R., Kristmannsdóttir, H., 2016. Mantle CO_2 degassing through the Icelandic crust: Evidence from carbon isotopes in groundwater. Geochim. Cosmochim. Acta 191, 300–319.

Stefánsson, A., Hilton, D.R., Sveinbjörnsdóttir, Á.E., Torssander, P., Heinemeier, J., Barnes, J.D., Ono, S., Halldórsson, S.A., Fiebig, J., Arnórsson, S., 2017. Isotope systematics of Icelandic thermal fluids. J. Volcanol. Geotherm. Res. 337, 146–164.

Sveinbjornsdottir, A.E., Coleman, M.L., Yardley, B.W.D., 1986. Origin and history of hydrothermal fluids of the Reykjanes and Krafla geothermal fields, Iceland: A stable isotope study. Contrib. Mineral. Petrol. 94, 99–109.

Troch, J., Ellis, B.S., Harris, C., Bachmann, O., Bindeman, I.N., 2020. Low-δ^{18}O silicic magmas on Earth: A review. Earth Sci. Rev. 208, 103299.

Viveiros, F., Chiodini, G., Cardellini, C., Caliro, S., Zanon, V., Silva, C., Rizzo, A.L., Hipólito, A., Moreno, L., 2020. Deep CO_2 emitted at Furnas do Enxofre geothermal area (Terceira Island, Azores archipelago). An approach for determining CO2 sources and total emissions using carbon isotopic data. J. Volcanol. Geotherm. Res. 401, 106968.

Werner, C., Fischer, T.P., Aiuppa, A., Edmonds, M., Cardellini, C., Carn, S., Chiodini, G., Cottrell, E., Burton, M., Shinohara, H., Allard, P., 2019. Carbon Dioxide Emissions from Subaerial Volcanic Regions: Two Decades in Review. In: Orcutt, B.N., Daniel, I., Dasgupta, R. (Eds.), Deep Carbon. Cambridge University Press, pp. 188–236.

Wiese, F., Fridriksson, T., Ármannsson, H., 2008. CO_2 fixation by calcite in high-temperature geothermal systems in Iceland. In: Report from the Iceland Geosurvey (ÍSOR), ÍSOR-2008/003, Reykjavik.